Monthly Notices of the ROYAL ASTRONOMICAL SOCIETY

MNRAS **488,** 164–182 (2019)
Advance Access publication 2019 June 4

doi:10.1093/mnras/stz1533

The dust content of the Crab Nebula

I. De Looze [1,2★] M. J. Barlow [2] R. Bandiera [3] A. Bevan [2] M. F. Bietenholz [4,5] H. Chawner,[6] H. L. Gomez,[6] M. Matsuura [6] F. Priestley[2] and R. Wesson[2]

[1]*Sterrenkundig Observatorium, Ghent University, Krijgslaan 281 S9, B-9000 Gent, Belgium*
[2]*Department of Physics & Astronomy, University College London, Gower Street, London WC1E 6BT, UK*
[3]*Osservatorio Astrofisico di Arcetri, Largo E. Fermi 5, I-50125 Firenze, Italy*
[4]*Hartebeesthoek Radio Observatory, PO Box 443, Krugersdorp 1740, South Africa*
[5]*Department of Physics and Astronomy, York University, Toronto, M3J 1P3 ON, Canada*
[6]*School of Physics and Astronomy, Cardiff University, Queens Buildings, The Parade, Cardiff CF24 3AA, UK*

Accepted 2019 May 31. Received 2019 May 20; in original form 2019 March 11

ABSTRACT

We have modelled the near-infrared to radio images of the Crab Nebula with a Bayesian SED model to simultaneously fit its synchrotron, interstellar (IS), and supernova dust emission. We infer an IS dust extinction map with an average $A_V = 1.08 \pm 0.38$ mag, consistent with a small contribution ($\lesssim$22 per cent) to the Crab's overall infrared emission. The Crab's supernova dust mass is estimated to be between 0.032 and 0.049 $M_\odot$ (for amorphous carbon grains) with an average dust temperature $T_{dust} = 41 \pm 3$ K, corresponding to a dust condensation efficiency of 8–12 per cent. This revised dust mass is up to an order of magnitude lower than some previous estimates, which can be attributed to our different IS dust corrections, lower SPIRE flux densities, and higher dust temperatures than were used in previous studies. The dust within the Crab is predominantly found in dense filaments south of the pulsar, with an average V-band dust extinction of $A_V = 0.20$–0.39 mag, consistent with recent optical dust extinction studies. The modelled synchrotron power-law spectrum is consistent with a radio spectral index $\alpha_{radio} = 0.297 \pm 0.009$ and an infrared spectral index $\alpha_{IR} = 0.429 \pm 0.021$. We have identified a millimetre excess emission in the Crab's central regions, and argue that it most likely results from two distinct populations of synchrotron emitting particles. We conclude that the Crab's efficient dust condensation (8–12 per cent) provides further evidence for a scenario where supernovae can provide substantial contributions to the IS dust budgets in galaxies.

Key words: key words: radiation mechanisms: non-thermal – supernovae: individual: Crab Nebula – ISM: supernova remnants.

1 INTRODUCTION

Early dust formation in the Universe (Watson et al. 2015; Laporte et al. 2017; Hashimoto et al. 2018) has been suggested to result from an efficient condensation of dust species in the aftermaths of core-collapse supernovae (CCSNe), requiring each supernova remnant (SNR) to produce a net dust mass ranging between 0.1 and 1 $M_\odot$ (Morgan & Edmunds 2003; Dwek, Galliano & Jones 2007). Core-collapse nucleation models are able to accommodate high dust condensation efficiencies (e.g. Todini & Ferrara 2001; Nozawa et al. 2010; Sarangi & Cherchneff 2015; Sluder, Milosavljević & Montgomery 2018; Marassi et al. 2019), but only during recent years have we been able to observationally confirm the hypothesis of CCSNe being dust factories by detecting the far-infrared (FIR) and sub-millimetre (submm) emission of up to 0.7 $M_\odot$ of dust in several Galactic SNRs (Barlow et al. 2010; Gomez et al. 2012; Arendt et al. 2014; De Looze et al. 2017; Temim et al. 2017; Rho et al. 2018; Chawner et al. 2019) and in SN 1987A (Matsuura et al. 2011; Indebetouw et al. 2014; Matsuura et al. 2015), using the *Herschel* Space Observatory (Pilbratt et al. 2010) and the Atacama Large Millimetre Array (ALMA). Recent dust masses inferred for a handful of mostly extragalactic SNRs by probing the effects of dust absorption and scattering on the optical line emission profiles of supernova ejecta, were similarly high (Bevan & Barlow 2016; Bevan, Barlow & Milisavljevic 2017; Bevan et al. 2019).

In this paper, we study the formation of dust in the Crab Nebula, a Galactic pulsar wind nebula (PWN) located at a distance of

★ E-mail: idelooze@star.ucl.ac.uk, ilse.delooze@ugent.be

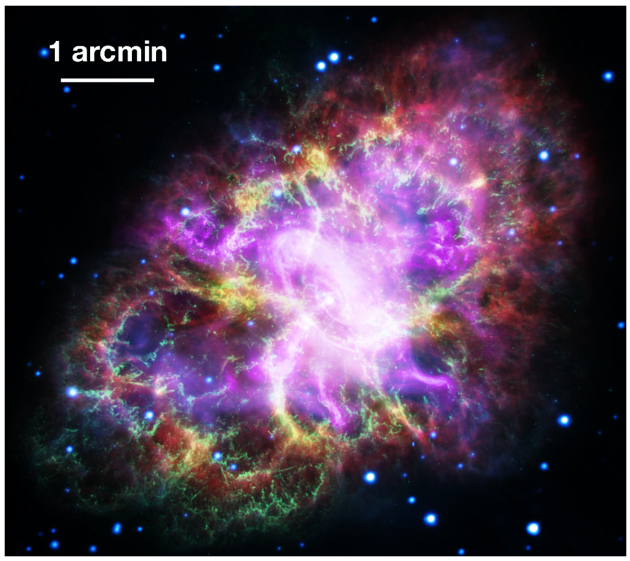

Figure 1. Composite image of the Crab Nebula combining data from five different wavelength domains: radio (red, Very Large Array), infrared (yellow, *Spitzer* Space telescope), optical (green, *Hubble* Space Telescope), ultraviolet (blue, *XMM–Newton*), and X-ray (purple, *Chandra* X-ray Observatory). Image credits: NASA, ESA, NRAO/AUI/NSF, and G. Dubner (University of Buenos Aires).

2 kpc[1] (Trimble 1968). The Crab Nebula is believed to be the remnant of a supernova of type II-P from a 8–11 $M_\odot$ progenitor star (MacAlpine & Satterfield 2008; Smith 2013) which exploded in 1054 AD. The Crab Nebula is one of the brightest radio sources and best-studied objects in the sky, with most of the emission at various wavelengths powered by the enormous amounts of energy released by the Crab's central pulsar. The observable part of the Crab Nebula is shaped by a PWN ploughing into more extended supernova ejecta (Chevalier 1977; Hester 2008). The Crab Nebula consists of the Crab pulsar, embedded in a synchrotron nebula, which emits from X-ray to radio wavelengths (see Fig. 1 for a composite image of the Crab Nebula) and consists of a magnetized relativistic plasma energized by the shocked pulsar wind. Embedded in this synchrotron nebula, there is a network of filaments composed of thermal ejecta which have been detected from optical to infrared wavebands in a range of ionization states (Davidson 1979; Graham, Wright & Longmore 1990; Blair et al. 1992; Temim et al. 2006, 2012). Spectroscopic studies of these filaments (Miller 1978; Smith 2003; MacAlpine et al. 2007) have been interpreted with models dominated by helium, with a helium mass fraction of 85–90 per cent, and enhanced mass fractions for carbon, oxygen, neon, sulphur, and argon, while nitrogen is depleted (Satterfield et al. 2012; Owen & Barlow 2015). The C/O mass ratios above unity remain unexplained by current CCSN nucleosynthesis models, but suggest that the Crab Nebula is predominantly carbon-rich.

These filaments also contain dust detected either in extinction (Sankrit et al. 1998; Grenman, Gahm & Elfgren 2017) or through thermal dust emission in the infrared (Marsden et al. 1984; Green, Tuffs & Popescu 2004; Temim et al. 2006, 2012; Gomez et al. 2012). Some of the dust also appears to be associated with dusty globules, spread across the outer part of the remnant, with sizes unresolved at current instrumental resolutions. In the pre-*Herschel* era, the Crab dust masses inferred based on observations from *IRAS* (0.005–0.03 $M_\odot$, Marsden et al. 1984), *ISO* + SCUBA (0.02–0.07 $M_\odot$, Green et al. 2004), and *Spitzer* (1.2–5.6 $\times$ 10^{-3} $M_\odot$ of silicate dust, Temim et al. 2006, 2012) remained below the dust mass production efficiency required to account for dusty galaxies observed in the early Universe. However, a total integrated analysis of *Herschel* observations out to FIR wavelengths, including a large set of ancillary near-infrared to radio observations to account for synchrotron contamination, resulted in $0.24^{+0.32}_{-0.08}$ $M_\odot$ of $T = 28$ K silicate dust, or more likely 0.11 ± 0.01 $M_\odot$ of $T = 34$ K carbon dust (Gomez et al. 2012), or a mixture of 0.14 and 0.08 $M_\odot$ of silicate and carbon dust. Temim & Dwek (2013), instead, estimated a dust mass of $0.019^{+0.010}_{-0.003}$ $M_\odot$ for a different type of carbonaceous grains with an average dust temperature of $T_{\rm dust} = 56 \pm 2$ K. Based on a combination of photoionization and dust radiative transfer modelling, Owen & Barlow (2015) inferred a mass of 0.18–0.27 $M_\odot$ of clumped amorphous carbon dust, or mixed models with 0.11–0.13 $M_\odot$ and 0.39–0.47 $M_\odot$ of amorphous carbon and silicate dust, respectively, within the limits of their model uncertainties.

In this paper, we present a spatially resolved analysis of the *Herschel* observations, as well as a large ancillary data set extending from near-infrared to radio wavelengths in order to disentangle the supernova dust emission from the synchrotron radiation that dominates the Crab's emission at nearly all wavelengths. In Section 2, we present the *Herschel* observations and ancillary data sets, and the different pre-processing steps that were applied to the data. In Section 3, we present total integrated photometric measurements, describe the model used to fit the Crab's total integrated flux densities, and discuss the model contributions to various wavebands. Similarly, the resolved modelling approach is described in Section 4. Our results for the synchrotron model, supernova dust mass and composition, and mm excess emission are discussed in detail in Sections 5–7, respectively. Finally, our conclusions are summarized in Section 8. In the Appendices, we outline the specifics of our Bayesian spectral energy distribution (SED) modelling method (see Appendix A), discuss the Bayesian model residuals (see Appendix B) and present our model estimation of the interstellar medium (ISM) dust contribution (see Appendix C). Appendix D discusses alternative scenarios that could contribute to the mm excess emission in the Crab Nebula. In Appendix E, we investigate whether the supernova dust model results depend on the assumed synchrotron spectrum, by exploring a more realistic evolutionary synchrotron model. Additional figures are assembled in Appendix F.

2 OBSERVATIONS AND DATA HANDLING

2.1 Herschel observations

The Crab Nebula was observed with the *Herschel* PACS and SPIRE instruments as part of the Guaranteed Time (GT) programme MESS (Mass-loss of Evolved StarS, PI: M. Groenewegen, Groenewegen et al. 2011). The PACS and SPIRE photometric data sets from the MESS programme have been presented in detail by Gomez et al. (2012) and Owen & Barlow (2015). In addition, the Crab Nebula was observed as part of PACS photometric calibration observations (ObsIDs 1342183905–1342183912). Table 1 provides an overview

[1]This distance measurement to the Crab is quite uncertain, and a recent GAIA study of the central pulsar has suggested that the distance to the Crab might be underestimated (Fraser & Boubert 2019). However, since this GAIA measurement is also quite uncertain we adopt in this paper the canonical distance of 2 kpc, which has most commonly been used.

Table 1. Overview of the observation identification numbers (ObsIDs), observing dates, central coordinate positions, and total observing times for the *Herschel* PACS and SPIRE photometric observations of the Crab Nebula.

Object	ObsID	Date	OD [y-m-d]	RA (J2000) [^{h} ^{m} ^{s}]	Dec. (J2000) [$^\circ$ $'$ $''$]	Obs. time [s]
			PACS photometry			
M 1	1342183905	2009-09-15	124	05:34:31.27	22:01:05.46	2221
M 1	1342183906	2009-09-15	124	05:34:31.27	22:01:05.46	2221
M 1	1342183907	2009-09-15	124	05:34:31.32	22:00:47.06	2221
M 1	1342183908	2009-09-15	124	05:34:31.32	22:00:47.06	2221
M 1	1342183909	2009-09-15	124	05:34:31.31	22:01:03.79	2221
M 1	1342183910	2009-09-15	124	05:34:31.31	22:01:03.79	2221
M 1	1342183911	2009-09-15	124	05:34:31.40	22:00:47.90	2221
M 1	1342183912	2009-09-15	124	05:34:31.40	22:00:47.90	2221
M 1	1342204441	2010-09-13	487	05:34:31.86	22:01:03.98	1671
M 1	1342204442	2010-09-13	487	05:34:31.85	22:01:03.85	1671
M 1	1342204443	2010-09-13	487	05:34:31.86	22:01:03.98	1671
M 1	1342204444	2010-09-13	487	05:34:31.85	22:01:03.85	1671
			SPIRE photometry			
M 1	1342191181	2010-02-25	287	05:34:32.42	22:00:50.89	4555

with details (i.e. ObsID, exposure time, central pointing) of the different sets of *Herschel* photometric observations.

The PACS photometric data from the MESS programme were obtained in scan-map mode with a scan speed of 20 arcsec s^{-1} and scan length of 22 arcmin. A pair of two orthogonal cross-scans were observed in each waveband combination blue+red (70 + 160 μm) and green + red (100 + 160 μm).[2] The PACS calibration observations covered a smaller region (16 × 16 arcmin^2) compared to the 25 × 25 arcmin^2 field of view of the MESS observations, and the scan-mapping was done at a slow speed of 10 arcsec s^{-1}. Due to the different observing modes used for both sets of PACS observations, and the different 1/*f* noise patterns in their maps, we reduced the PACS data from each observing program separately. The PACS data were reduced with the latest version of `HIPE` v14.0 (Ott 2010) using the standard `scanamorphos` (Roussel 2013) data reduction script that requires the Level 1 data from the *Herschel* Science Archive (HSA) and reduces it to Level 2.5. The reduced maps from the two programs were combined into a single map for each waveband after rebinning of both maps to the same pixel grid. The FWHM of the PACS beam in the combined image corresponds to 5.6 arcsec, 6.8 arcsec, and 11.4 arcsec at 70, 100, and 160 μm, respectively (see PACS Observers' Manual[3]). We have assumed a calibration uncertainty of 7 per cent in each of the PACS wavebands (Balog et al. 2014).

The SPIRE maps were obtained in 'Large Map' mode with a scan length of 30 arcmin and scan speed of 30 arcsec s^{-1} resulting in a map of size 32 × 32 arcmin^2. Three pairs of orthogonal cross-scans were observed to reduce the 1/*f* noise in the combined maps. The SPIRE data were reduced with `HIPE` version v14.0.0 using the standard pipeline for the SPIRE Large Map Mode. As part of the data processing, the *Planck* HFI maps at 857 and 545 GHz (350 and 550 μm) were used to determine the absolute scaling of the SPIRE maps with extended emission. The FWHM of the SPIRE beam in the final images corresponds to 18.2 arcsec, 24.9 arcsec, and 36.3 arcsec at 250, 350, and 500 μm, respectively (see SPIRE Observers' Manual[4]). Calibration errors of 5.5 per cent were assumed for SPIRE (SPIRE Observers' Manual, Bendo et al. 2013). More details on the various *Herschel* PACS and SPIRE data reduction steps can be found in De Looze et al. (2017).

2.2 Ancillary data

2.2.1 Spitzer

The Infrared Array Camera (IRAC; Fazio et al. 2004), Multiband Imaging Photometer (MIPS; Rieke et al. 2004), and Infrared Spectrograph (IRS; Houck et al. 2004) on board the *Spitzer* Space Telescope (Werner et al. 2004) have observed the Crab Nebula as part of the Gehrz Guaranteed Time Observing Program (Program ID: 130). A detailed description of the observations, data reduction, and analysis of the *Spitzer* data have been presented by Temim et al. (2006). We retrieved the IRAC and MIPS 24 μm final data products from the *Spitzer* Heritage archive.[5] Extended source correction factors were applied to the IRAC images according to the recommendations of the IRAC Instrument Handbook. Flux calibration uncertainties for extended sources are assumed to be 10 per cent in the IRAC bands (IRAC Instrument Handbook[6]), and 4 per cent and 10 per cent in the MIPS 24 (Engelbracht et al. 2007) and MIPS 70 μm (Gordon et al. 2007) bands.

The *Spitzer* IRS low-resolution spectra were retrieved from the Combined Atlas of Sources with *Spitzer* IRS Spectra (CASSIS; Lebouteiller et al. 2011) at the same three positions used by Temim et al. (2012) (with AORKEYs '12634624', '16200704', and '16201216') to explore the effect of line contributions to the near- and mid-infrared continuum wavebands. Due to the extended nature of the Crab's emission, we opted for the 'tapered column' (default) extraction, which accounts for the increasing size of the point spread function (PSF) with wavelength while extracting fluxes.

[2]Due to this observing mode, the PACS 160 μm map has twice the integration time of the 70 and 100 μm maps.
[3]http://herschel.esac.esa.int/Docs/PACS/html/pacs_om.html
[4]http://herschel.esac.esa.int/Docs/SPIRE/html/spire_om.html
[5]http://sha.ipac.caltech.edu/applications/Spitzer/SHA/
[6]http://irsa.ipac.caltech.edu/data/SPITZER/docs/irac/-iracinstrumenthandbook/

2.2.2 *WISE*

The Crab Nebula was observed as part of the all-sky Wide-field Infrared Survey Explorer (*WISE*; Wright et al. 2010) in four photometric bands at 3.4, 4.6, 11.6, and 22.0 μm at angular resolutions of FWHM = 6.1 arcsec, 6.4 arcsec, 6.5 arcsec, and 12 arcsec, respectively. We retrieved *WISE* maps from the NASA/IPAC Infrared Science Archive. These were converted from DN units to Vega magnitudes using the photometric zero-point magnitudes as specified in the image headers. The zero magnitude flux densities (see explanatory supplement to the NEOWISE data release products) were applied to convert these images from magnitudes to flux densities in Jy. We assumed calibration uncertainties of 2.4 per cent, 2.8 per cent, 4.5 per cent, and 5.7 per cent (Jarrett et al. 2013), respectively.

2.2.3 *Millimetre and radio observations*

In the millimetre wavelength range, we used the Goddard-IRAM Superconducting 2 Millimetre Observer (GISMO; Staguhn et al. 2006) 2 mm data observed on the IRAM 30 m telescope, and Multiplexed Squid TES Array at Ninety GHz (MUSTANG; Dicker et al. 2008) 3.3 mm observations obtained with the Green Bank Telescope (GBT). The data sets, observational details and data reduction strategy have been presented in detail in Arendt et al. (2011). At 2 mm, Arendt et al. (2011) reported a total integrated flux density of 244 ± 24 Jy. The total flux density at 3.3 mm was less well constrained due to the small field of view (FOV = 40 arcsec × 40 arcsec) and the loss of large-scale emission. We relied on the total integrated millimetre–centrimetre–radio spectrum of the Crab Nebula and the best-fitting synchrotron spectrum with spectral index of $\alpha = 0.297$ (see Section 5) to calibrate the 2 and 3.3 mm images to the same epoch as the *Planck* observations. The total integrated flux densities at 2 and 3 mm were updated to 242.6 ± 24.3 and 256.7 ± 25.7 Jy, respectively, after applying corrections for the Crab's decrease in flux (see later). We have assumed uncertainties of 10 per cent on these flux densities to account for uncertainties in the background subtraction, absolute calibration, rescaling, and expanding of the image to a recent epoch (see Section 2.3), and the possible lack of flux detected on large scales.

In addition, we used the MAMBO 1.3 mm map obtained with the IRAM 30 mm telescope by Bandiera, Neri & Cesaroni (2002). Aperture photometry, rescaling, and expanding the 1.3 mm map to the present epoch resulted in a total integrated flux density of 254.2 Jy at 1.3 mm. We have assumed a conservative uncertainty factor of 20 per cent following the recommendations of Bandiera et al. (2002).

A radio map at 1.4 GHz of the Crab Nebula was assembled from observations between 1987 and 1988 with the Very Large Array (VLA) in all four configurations (Bietenholz & Kronberg 1990). More details on the observations and data reduction can be retrieved from Bietenholz & Kronberg (1990). We updated the VLA 1.4 GHz image from B1950 to J2000 coordinates. Due to the expansion of the SNR, we have furthermore expanded the SNR's emission spatially by 3.11 per cent accounting for the expansion rate of 0.135 per cent per year (Bietenholz et al. 2015) between the observing date (1987) and the reference epoch of *WISE*, *Herschel*, and *Planck* observations (2010).[7] Total integrated flux densities of 599.3 and 833.77 Jy were inferred at 4.8 and 1.4 GHz, respectively. Uncertainty factors of 20 per cent were applied to account for uncertainties in the primary beam correction, absolute calibration, and rescaling and resizing of the image to the 2010 reference epoch. Table 2 provides an overview of the observational details for these millimetre and radio observations.

[7]The expansion does not affect the total integrated photometry measurements.

2.2.4 *Planck*

The *Planck* 'aperture photometry' measurements for the Crab Nebula presented by Planck Collaboration XXXI (2016a) were retrieved. Alternative *Planck* flux measurements for the Crab Nebula are reported in the Second *Planck* Catalogue of Compact Sources (PCCS2; Planck Collaboration XXVI 2016b), but were considered inadequate due to the extended nature of the SNR with respect to the *Planck* beam sizes.

2.3 Correction for flux decay

Due to changes in the energy distribution of the underlying relativistic particles, the radio synchrotron emission decreases with time. To compare the Crab Nebula's observations obtained at different epochs, we scaled the observed images and/or flux densities to account for the secular decay of the Crab Nebula's emission by −0.202 per cent per year to a reference epoch of 2010. This flux decay rate was inferred by Bietenholz et al. (2015) as the weighted average of earlier estimates from Aller & Reynolds (1985), Vinyaikin (2007), and Weiland et al. (2011). Our applied rate assumes that the flux decay is wavelength independent, which seems to be largely supported by recent studies (Vinyaikin 2007; Weiland et al. 2011). To correct the resolved maps, we assume that the flux decay does not have any spatial dependence. We neglect any secular variations on local scales which appear to be present predominantly within a 1 arcmin region around the pulsar and can account for changes up to 10 per cent of the peak flux (Bietenholz et al. 2015).

2.4 Line contamination

We corrected the MIPS 24 μm images and total integrated flux densities for line contamination based on the recommended values reported by Gomez et al. (2012), who accounted for line contributions of 43 ± 6 per cent[8] in the MIPS 24 μm waveband, and 4.9 ± 0.05 per cent and 8.7 ± 0.3 per cent in the PACS 70 and PACS 100 μm wavebands. We assumed the same correction factor (43 ± 6) for the WISE 22 μm waveband. We estimated an average contribution of 16 ± 8 per cent from [Ar III] 8.99 μm and [Ar II] 6.99 μm line emission to the IRAC 8 μm waveband based on the *Spitzer* IRS spectra extracted from three dense filaments in the southern half of the Crab. We attempted to similarly quantify the line contributions to the WISE 12 μm waveband, and found that the [Ne II] 12.81 μm, [Ne V] 14.32 μm, [Ne III] 15.56 μm, and [S IV] 10.51 μm lines account for a non-negligible portion of the WISE 12 μm emission, with contributions that significantly vary throughout the remnant (possibly due to the sensitivity of these lines to the local ionization conditions). We therefore omitted the

[8]This value reported by Temim et al. (2012) accounts for the contribution of line emission after synchrotron subtraction. Based on our best-fitting synchrotron model, this value translates into a 24 ± 6 per cent contribution of line emission to the total integrated MIPS 24 μm flux density.

Table 2. Overview of the ancillary data sets of the Crab Nebula with references: (1) Bandiera et al. (2002); (2) Arendt et al. (2011); (3) Bietenholz & Kronberg (1990); (4) Bietenholz & Kronberg (1991).

Instrument	Wavelength	Telescope	Obs date	FWHM	Reference
		Millimetre + radio data			
MAMBO	1.3 mm	IRAM 30 m	Dec 1998 + Feb 2000	10.5 arcsec	(1)
GISMO	2 mm	IRAM 30 m	Nov 2007	16.7 arcsec	(2)
MUSTANG	3.3 mm	GBT	Feb 2008	9 arcsec	(2)
VLA	4.8 GHz	VLA	1987	5 arcsec[a]	(3,4)
VLA	1.4 GHz	VLA	1987	5 arcsec[a]	(3,4)

[a]VLA images had been smoothed from their original resolution of 1.8 arcsec × 2.0 arcsec to a resolution of 5 arcsec.

WISE 12 μm images from our analysis to prevent the introduction of a bias in the fitting results driven by poorly constrained line contributions in the WISE 12 μm waveband. The PACS 160 μm and three SPIRE wavebands were found to have a negligible (< 1 per cent) contribution from line emission to the broad-band continuum flux densities. Due to the limited spatial coverage of *Spitzer* IRS spectra, *Herschel* PACS, and SPIRE spectroscopic observations, and the insufficient spatial resolution of ISO observations, we were unable to infer spatial variations in line-to-continuum ratios across the remnant.

2.5 Image processing

To compare observations obtained by various instruments with different intrinsic resolutions, we subtracted a background from all *Herschel* and ancillary images using a set of background apertures with radius equal to 4 × FWHM randomly placed in the background regions of the respective images. Convolution of the images to the SPIRE 500 μm image resolution was performed using the kernels from Aniano et al. (2011), after which images were regridded to the size (14 arcsec × 14 arcsec) of pixels in the SPIRE 500 μm image.

The *Spitzer* and *WISE* images were corrected for Galactic foreground extinction. We adopted a reddening of $E(B-V) = 0.39 \pm 0.03$ along the line of sight to the Crab Nebula at the assumed distance of the remnant (i.e. 2 kpc) from the 3D dust reddening map constructed by Green et al. (2015) based on Pan-STARRS1 (PS1) and 2MASS photometry for 800 and 200 million stars, respectively. For a Galactic reddening law with $R_V = 3.1$ (Fitzpatrick 1999), we derive a V-band dust extinction of $A_V = 1.21$, which compares reasonably well to the reddening ($A_V = 1.6 \pm 0.2$) inferred from optical spectrophotometric measurements of two Crab filaments (Miller 1973). We apply dust extinction correction factors of 1.06, 1.04, 1.03, and 1.02 to the IRAC 3.6, 4.5, 5.8, and 8.0 μm bands. The latter factors are somewhat lower compared to the correction factors of 1.11 and 1.08 applied to the IRAC 3.6 and 4.5 μm channels by Temim et al. (2012), and was based on the hydrogen column density of the foreground gas derived from soft X-ray absorption (Willingale et al. 2001).

2.6 Colour correction

We did not apply colour corrections to the observed flux densities, as the model SEDs are convolved with the appropriate filter response curves[9] before comparing the model to the observations during every step of the Bayesian fitting algorithm. We did apply a correction factor for the dependence of the effective SPIRE beam area on the shape of the spectrum due to the absolute SPIRE calibration in units of flux density per beam. From the different model components contributing to the SPIRE wavebands, we have calculated the spectral index, α_S, in $I_S(\nu) = I_S(\nu_0)(\nu/\nu_0)^{\alpha_S}$, where $I_S(\nu_0)$ is the surface brightness at a reference frequency ν_0. We then applied the SPIRE beam area correction factors for different values of α_S based on the tabulated values in table 5.4 of the SPIRE Observers' Manual.

[9]We were not able to retrieve filter response curves for the millimetre and radio observations of the Crab Nebula, and have determined monochromatic flux densities in those wavebands.

3 TOTAL INTEGRATED SPECTRUM OF THE CRAB NEBULA

3.1 Total integrated flux densities

We have measured the total emission of the Crab Nebula in various wavebands from the near-infrared to radio wavelength domain within an elliptical aperture (245 arcsec × 163 arcsec) centred on the Crab pulsar (RA: $05^h34^m31.94^s$ Dec.: $22^\circ0'52''.18$) with a position angle of 40° (see Table 3, second column). Due to our choice of aperture, we can compare our *Herschel* photometric measurements to the flux densities reported in Gomez et al. (2012) (see Table 3). For most wavebands, both sets of flux densities are consistent within the errors, with the exception of the PACS 160 μm and SPIRE 500 μm bands. Our PACS 160 μm flux density is 17.6 per cent higher, while the SPIRE 500 μm flux density inferred here is 17 per cent lower compared to the Gomez et al. (2012) results. At PACS 160 μm, the (minor) difference is thought to arise from the deeper imaging of the nebula (with the inclusion of the deep PACS calibration images), as the applied data reduction techniques were similar in both cases. The slightly lower SPIRE 500 μm flux density could result from updated SPIRE beam size measurements (resulting in a decrease in flux density of 8 per cent) or the use of *Planck* data to recover the absolute calibration for extended structures, or a combination of both effects. Nehmé, Kassounian & Sauvage (2019) infer a SPIRE 500 μm flux density (103.3 ± 8.4 Jy) based on a 'flux threshold' method to identify the Crab's emission (rather than aperture photometry) and after subtracting any background and interstellar (IS) dust emission along the Crab's line of sight, which is consistent with our background-subtracted and ISM dust-corrected SPIRE 500 μm flux density (100.3 ± 6.8 Jy).

3.2 Model description

The near-infrared to radio emission of the Crab Nebula is dominated by four emission components: synchrotron, supernova dust, IS dust, and an (as yet) unidentified mechanism at millimetre wavebands.

Table 3. Overview of the total integrated photometry for the Crab Nebula measured within an elliptical aperture with semimajor and -minor axes 245 arcsec × 163 arcsec centred on the position of the pulsar (RA, Dec.) = (RA: $05^h34^m31.94^s$ Dec.: $22^\circ0'52''.18$) with a position angle of 40° (to match the same flux region as assumed in Gomez et al. 2012). Columns 1, 2, and 4 list the waveband, total, and emission line flux densities, respectively. Total flux densities were extinction corrected, and were already scaled to our 2010 reference epoch. Columns 5, 7, 8, and 10 report the emission due to synchrotron radiation, interstellar (IS) dust emission, SN dust emission and mm excess emission, respectively. The SN dust flux densities were inferred from the total integrated model for amorphous carbon grains 'a-C' (see Section 3). The values in parentheses represent the contributions of the different emission components relative to the total model flux, which have also been displayed in Fig. 4. Because the Bayesian model is fitting the observed flux densities within the limits of uncertainty, the fractional contributions might not exactly add up to a 100 per cent. Columns 3, 6, and 9 present the total, synchrotron, and SN dust flux densities, inferred by Gomez et al. (2012) (G12), for comparison. A dash in the table indicates that the contributions are insignificant (i.e. lower than 0.01 per cent), while a forward slash is used for wavebands that were not used to constrain our model.

(1) Waveband	(2) Total Obs. F_ν Jy	(3) Total Obs. F_ν Jy (G12)	(4) Line Obs. F_ν Jy [per cent]	(5) Synchr. Model F_ν Jy [per cent]	(6) Synchr. Model F_ν Jy (G12)	(7) IS dust Model F_ν Jy [per cent]	(8) SN dust Model F_ν [per cent]	(9) SN dust Model F_ν Jy (G12)	(10) Mm excess Model F_ν Jy [per cent]
IRAC 3.6 μm	12.0 ± 1.3	12.6 ± 0.2	–	$11.9^{+0.8}_{-0.6}$ [99.2 per cent]	13.2	–	–	–	–
IRAC 4.5 μm	14.5 ± 1.6	14.4 ± 0.3	–	$13.1^{+0.8}_{-0.6}$ [90.3 per cent]	14.5	–	–	–	–
IRAC 5.8 μm	15.3 ± 2.2	16.8 ± 0.1	–	$14.5^{+1.0}_{-0.6}$ [94.8 per cent]	16.1	–	–	–	–
IRAC 8 μm	19.7 ± 2.0	18.3 ± 0.1	–	$16.6^{+1.2}_{-0.7}$ [84.3 per cent]	18.5	–	$0.05^{+0.04}_{-0.05}$ [0.3 per cent]	–	–
WISE 3.4 μm	11.2 ± 0.3	12.9 ± 0.6	–	$11.6^{+0.8}_{-0.6}$ [103.6 per cent]	13.1	–	–	–	–
WISE 4.6 μm	14.1 ± 0.4	14.7 ± 0.8	–	$13.2^{+0.8}_{-0.6}$ [93.6 per cent]	14.6	–	–	–	–
WISE 12 μm	32.2 ± 1.4	/	/	/	/	/	/	/	/
WISE 22 μm	62.0 ± 3.7	60.3 ± 3.5	14.6 ± 3.7 [23.6 per cent]	$25.6^{+2.8}_{-1.0}$ [41.3 per cent]	28.1	$0.5^{+0.5}_{-0.3}$ [0.8 per cent]	$17.8^{+10.3}_{-11.4}$ [28.7 per cent]	–	–
MIPS 24 μm	58.7 ± 2.9	59.8 ± 6.0	13.9 ± 3.5 [23.6 per cent]	$26.3^{+3.0}_{-1.0}$ [44.8 per cent]	29.2	$0.5^{+0.6}_{-0.3}$ [0.9 per cent]	$20.9^{+13.9}_{-11.8}$ [35.6 per cent]	17.2	–
PACS 70 μm	220.9 ± 19.5	212.8 ± 21.3	10.8 ± 0.1 [4.9 per cent]	$41.8^{+7.4}_{-1.5}$ [18.9 per cent]	45.6	$2.6^{+4.2}_{-1.6}$ [1.2 per cent]	$168.2^{+58.4}_{-63.2}$ [76.1 per cent]	156.8	–
MIPS 70 μm	183.9 ± 18.6	208.0 ± 33.3	/	/	45.6	/	/	/	/
PACS 100 μm	208.2 ± 18.5	215.2 ± 21.5	18.1 ± 0.6 [8.7 per cent]	$48.4^{+9.5}_{-1.7}$ [23.2 per cent]	52.9	$9.6^{+13.9}_{-5.9}$ [4.6 per cent]	$142.2^{+40.0}_{-55.9}$ [68.3 per cent]	143.6	$0.03^{+1.10}_{-0.03}$ [0.01 per cent]
PACS 160 μm	166.7 ± 14.0	141.8 ± 14.2	–	$58.9^{+13.2}_{-2.2}$ [35.3 per cent]	64.3	$23.9^{+24.9}_{-13.3}$ [14.3 per cent]	$69.9^{+35.6}_{-35.7}$ [41.9 per cent]	77.5	$0.3^{+3.4}_{-0.3}$ [0.2 per cent]
SPIRE 250 μm	110.7 ± 6.7	103.4 ± 7.2	–	$70.2^{+17.6}_{-2.7}$ [63.4 per cent]	77.5	$23.9^{+19.1}_{-12.3}$ [21.6 per cent]	$25.1^{+22.2}_{-14.3}$ [22.7 per cent]	25.9	$1.6^{+7.7}_{-1.6}$ [1.4 per cent]
SPIRE 350 μm	106.3 ± 6.0	102.4 ± 7.2	–	$81.0^{+22.0}_{-3.3}$ [76.2 per cent]	89.2	$14.7^{+10.0}_{-7.2}$ [13.8 per cent]	$10.4^{+12.8}_{-6.2}$ [9.8 per cent]	13.2	$5.0^{+12.5}_{-5.0}$ [4.7 per cent]
SPIRE 500 μm	107.0 ± 6.0	129.0 ± 9.0	–	$93.6^{+27.7}_{-4.1}$ [87.5 per cent]	103.5	$6.7^{+4.0}_{-3.1}$ [6.3 per cent]	$3.7^{+6.6}_{-2.2}$ [3.5 per cent]	10.1	$14.0^{+17.8}_{-14.0}$ [13.1 per cent]
GISMO 2 mm	242.6 ± 24.3	–	–	$170.6^{+58.3}_{-9.0}$ [70.3 per cent]	–	$0.1^{+0.1}_{-0.1}$ [0.04 per cent]	$0.06^{+0.26}_{-0.04}$ [0.02 per cent]	–	$78.9^{+34.8}_{-78.7}$ [32.5 per cent]
VLA 4.8 GHz	599.3 ± 125.7	–	–	$599.1^{+22.0}_{-25.5}$ [100.0 per cent]	–	–	–	–	–
VLA 1.4 GHz	833.8 ± 174.9	–	–	$861.9^{+54.6}_{-62.1}$ [103.4 per cent]	–	–	–	–	–

3.2.1 Interstellar dust contribution

We have estimated the contribution from IS dust based on 2033 neighbouring pixels dominated by ISM dust emission, and found a maximum contribution of 22 per cent in the SPIRE 250 μm waveband, and lower contributions in all other bands (see Appendix C). We have subtracted an average ISM dust contribution from the total integrated flux densities and from the individual pixels in the maps prior to the SED modelling. Uncertainties inherent to these ISM dust corrections were added in quadrature to the measurement uncertainties. The residual flux densities were then modelled with a three-component model aiming to reproduce the Crab's synchrotron radiation, warm and cold SN dust emission, and excess emission

in the millimetre wavelength range. We attempted to run models without a mm excess component, but those synchrotron + SN dust models tend to overestimate the SPIRE flux densities by a factor of 2 or more.

3.2.2 Synchrotron model

Synchrotron radiation is generally characterized by a non-thermal power-law spectrum ($F_\nu \propto \nu^\alpha$ for a given spectral index α). With the optical spectral index ($\alpha = 0.6$–1.0, Veron-Cetty & Woltjer 1993) being steeper than the radio one ($\alpha = 0.3$, Baars et al. 1977), a spectral break between 1 and 1000 μm was inferred (Marsden et al. 1984; Woltjer 1987), which is representative of the upper limit on the energy of the electron population. We have therefore modelled the synchrotron spectrum as a broken power-law spectrum:

$$F_\nu = \begin{cases} F_{\nu_0} \times \left(\frac{\nu}{\nu_0}\right)^{-\alpha_{\rm radio}} & (\text{if } \lambda \geq \lambda_{\rm break}) \\ F_{\nu_0} \times \left(\frac{\nu}{\nu_0}\right)^{-\alpha_{\rm IR}} \times a & (\text{if } \lambda < \lambda_{\rm break}) \end{cases}$$

with

$$a = \left(\frac{\nu_{\rm break}}{\nu_0}\right)^{-\alpha_{\rm radio}} \times \left(\frac{\nu_{\rm break}}{\nu_0}\right)^{+\alpha_{\rm IR}} \quad (2)$$

being a scaling factor that guarantees the continuity of the two power-law slopes, and where the reference frequency is chosen as $\nu_0 = 1.4$ GHz. The radio and IR spectral indices, $\alpha_{\rm radio}$ and $\alpha_{\rm IR}$, are allowed to vary uniformly between 0.1 and 0.4, and between 0.3 and 1.0, respectively. The model prior furthermore excludes any models for which $\alpha_{\rm IR} < \alpha_{\rm radio}$, to avoid unphysical models with a flattening of the synchrotron spectrum at IR wavelengths. As earlier values for the synchrotron break wavelength were poorly constrained, we assume a flat prior for $\lambda_{\rm break}$ within a large parameter space ranging from 20 μm to 2 cm. In addition, the normalization of the synchrotron spectrum, $F_{1.4\,\rm GHz}$ has a flat prior ranging between 300 and 3000 Jy.

As a monochromatic break, which is currently assumed in our broken power-law synchrotron model, will be too sharp to mimic an evolutionary synchrotron spectrum, we have tested how our modelling results (in particular the supernova dust masses) are affected by our simple synchrotron model assumption (see Appendix E for more info). More specifically, we have replaced our broken power-law spectrum with a synchrotron spectrum with a smooth evolutionary break. The evolutionary synchrotron model results in slightly worse fits to the total integrated Crab spectrum, in particular at submm wavelengths, with a reduced $\chi^2_{\rm dust} = 8.2$ compared to 1.2 for our broken power-law synchrotron model. Further refinement of this evolutionary synchrotron model will be deferred to future work, due to the complexity of the spatial and secular variations in the energy distribution of relativistic particles in the Crab. However, we have verified that our choice of synchrotron model does not affect the supernova dust model parameters, and therefore decided to apply a broken power-law synchrotron spectrum (which requires no prior assumptions about the energy distribution of electrons and its evolution with time in the Crab) for the modelling presented in the remainder of this work.

3.2.3 Supernova dust model

We have modelled the SN dust emission with a two-component warm + cold optically thin modified blackbody (MBB) model with a fixed dust composition, where the dust emission is given by

$$F_\nu = \frac{M_{\rm dust}}{D^2}\, \kappa_\nu\, B_\nu(T_{\rm dust}). \quad (3)$$

Rather than assuming a single dust mass absorption coefficient κ_{ν_0}, and assuming a power-law distribution $\kappa_\nu = \kappa_{\nu_0} \times (\nu/\nu_0)^\beta$ with dust emissivity index β, we have 'modified' the blackbody function based on the κ_ν spectrum inferred for several specific grain species. Due to the high abundance of carbon in the Crab Nebula (Owen & Barlow 2015), we have attempted to model the total integrated SED using various carbonaceous grain species: amorphous carbon 'AC1' and 'BE1' grains from Rouleau & Martin (1991), 'ACAR' and 'BE' grains from Zubko et al. (1996), and amorphous carbon a-C grains with band gap $E_{\rm g} = 0.1$ eV from Jones (2012a,b,c). We have furthermore explored a variety of other grain species: silicate-type grains ($MgSiO_3$, Dorschner et al. 1995; $Mg_{0.7}SiO_{2.7}$, Jäger et al. 2003) and pure iron grains (with sizes of $a = 0.1$ μm and 1 μm; private communication with T. Nozawa and E. Dwek). For silicate-type and carbonaceous grains, we have assumed a grain size of 1 μm. To verify the effect of our grain size assumption, we have also modelled the total integrated SED using amorphous carbon 'a-C' grains with a size $a = 0.1$ μm. Fig. 2 provides an overview of how the dust mass absorption coefficients vary as a function of infrared and submm wavelengths for the various grain species explored in this work, covering a wide range of dust emissivities and absolute dust opacities. The warm and cold dust temperatures are inferred from a flat prior with $T_{\rm warm} \in [40\,{\rm K}, 100\,{\rm K}]$ and $T_{\rm cold} \in [12\,{\rm K}, 60\,{\rm K}]$ with $T_{\rm warm} > T_{\rm cold}$. The logarithmic values of the cold and warm dust masses are sampled from $\log M_{\rm warm} \in [-7, 1]\log {\rm M}_\odot$ and $\log M_{\rm cold} \in [-4, 1]\log {\rm M}_\odot$.

3.2.4 Millimetre excess model

To model the millimetre excess emission, we assume the following spectrum:

$$F_\nu = F_{\rm mm,peak} * \exp\left(-\frac{\log(\nu/\nu_{\rm peak})^2}{2\sigma^2}\right), \quad (4)$$

which is fully characterized by its width (σ, with a flat prior between 0.1 and 1.0), peak frequency ($\nu_{\rm peak}$, with a flat prior between 30 and 400 GHz) and peak amplitude ($F_{\rm mm,\,peak}$, with a flat prior between 1 and 300 Jy). Due to the uncertain nature of the excess emission (see Section 7), we have opted for a rather generic functional form to fit the millimetre excess. In summary, we have a total of 11 free parameters in our model: four free parameters to model the synchrotron spectrum ($\alpha_{\rm radio}$, $\alpha_{\rm IR}$, $\lambda_{\rm break}$, $F_{1.4\,\rm GHz}$), four to model the supernova dust emission ($T_{\rm warm}$, $\log M_{\rm warm}$, $T_{\rm cold}$, $\log M_{\rm cold}$), and three to model the excess millimetre emission ($\nu_{\rm peak}$, σ, $F_{\rm mm,\,peak}$). Due to the large number of parameters, we have employed a Bayesian inference method coupled to a Markov Chain Monte Carlo algorithm to search the entire parameter space in an efficient way, and to reveal any parameter degeneracies (see Appendix A for a detailed description of the method).

Fig. 3 shows the best-fitting (i.e. maximum likelihood) model spectrum (black solid line) for 1 μm-sized amorphous carbon 'a-C' grains used to model the Crab's supernova dust emission, and with the emission of individual components (synchrotron, cold + warm SN dust and excess emission) indicated. The 1D and 2D posterior distributions for each of the parameters are presented in Fig. F1. We discuss the total integrated model results for synchrotron radiation, supernova dust emission, and millimetre excess emission in more detail in Sections 5–7, respectively.

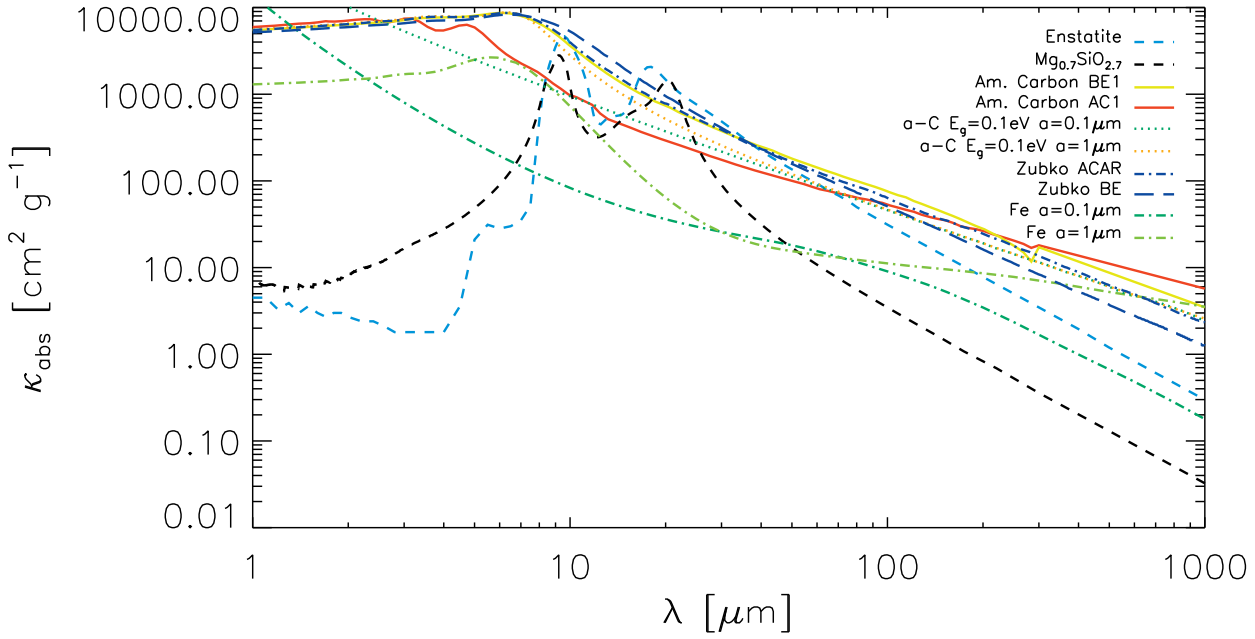

Figure 2. The variation as a function of wavelength in dust mass absorption coefficients, κ_{abs}, calculated based on Mie theory for spherical grains with sizes $a = 0.1$ and 1 μm, for different dust species. The legend in the top right corner clarifies the composition and grain size of the different dust species (if not specified, the grain size is assumed to be $a = 1$ μm).

3.3 Dominant emission mechanisms

The total integrated SED modelling results enable us to infer the model contributions of different emission mechanisms (line emission, synchrotron radiation, ISM dust emission, mm excess, SN dust emission) to each waveband. Fig. 4 provides an overview of the estimated contributions for our total integrated model with amorphous carbon 'a-C' grains for the SN dust. Most wavebands, from the near-infrared to submillimetre and radio wavelengths are dominated by synchrotron emission, except at mid- and FIR wavelengths. The IRAC 3.6 μm and VLA 1.4 GHz emission (and also VLA 4.8 GHz emission, not shown here) is modelled to originate from synchrotron radiation. At mm wavelengths, there is a non-negligible contribution from excess emission with a contribution of 33 per cent at 2 mm. Modelling the excess emission introduces a tail of excess emission that extends to submm wavelengths with 1, 5 and 13 per cent of excess emission contributions to the SPIRE 250, 350, and 500 μm wavebands, respectively. In addition, synchrotron radiation accounts for 63, 76, and 88 per cent of all emission in those respective wavebands, while SN dust emission is found to be responsible for 23 per cent, 10 per cent and 4 per cent of the submm emission. The total observed SPIRE flux densities are systematically overestimated by 9, 5, and 10 per cent in our model at 250, 350, and 500 μm, respectively. The overestimation might (in part) result from an overestimation of the mm excess contribution to the SPIRE wavebands due to the assumption of our spectrum (see equation 4) to model the excess emission. The SPIRE 500 μm emission is mostly arising from synchrotron radiation, with a negligible contribution from ISM dust and SN dust emission. The PACS 70, 100, and 160 μm wavebands are dominated by SN dust emission (contributing 76, 68, and 42 per cent, respectively), with a secondary contribution from synchrotron radiation (19, 23, and 35 per cent, respectively) and minor contributions from line emission at PACS 70 μm (5 per cent) and PACS 100 μm (9 per cent). At mid-infrared wavelengths, the SN dust emission drops to 36 per cent; synchrotron radiation (45 per cent) is the dominant emission mechanism at MIPS 24 μm, together with a non-negligible contribution from line emission (24 per cent). The contributions of the different components to the MIPS and PACS wavebands do not perfectly add up to 100 per cent, but remain within model and observational uncertainties.

4 RESOLVED MODELLING OF THE CRAB NEBULA

To study spatial variations in the synchrotron spectral indices, and the temperature and mass of SN dust, we have modelled the mid-infrared to radio observations of the Crab Nebula in our resolved map with 336 individual 14 arcsec × 14 arcsec (or 0.136^2 pc^2) pixels. Hereto, we have convolved sixteen images (IRAC 3.6, 4.5, 5.8, 8.0 μm; WISE 3.4, 4.6 and 22 μm, MIPS 24 μm, PACS 70, 100, and 160 μm, SPIRE 250, 350, 500 μm, 4.8 and 1.4 GHz) to the SPIRE 500 μm resolution, and corrected all images for line emission and an average contribution from ISM dust emission.

We applied a Bayesian inference method similar to the one used for the total integrated SED fit (see Section 3.2). Due to the fewer flux density constraints and lower signal to noise on a pixel-by-pixel basis, we restricted the model to include a two-component SN dust MBB model and a broken-power-law synchrotron component (see Table A1). Due to insufficient sampling of the mm spectrum on resolved scales, the parameters of the synchrotron and mm excess model components could not be constrained simultaneously.

We did not use the resolved images at mm wavelengths (1.3 mm, 2 mm, 3 mm) to constrain the Bayesian models. Instead, we produced model images at each of these wavelengths, and used those to study the resolved distribution of model excess emission in Section 7.1. We furthermore fixed the radio spectral index, which is otherwise hard to constrain with only two data points in the mm to radio wavelength domain. We relied on the total integrated SED-

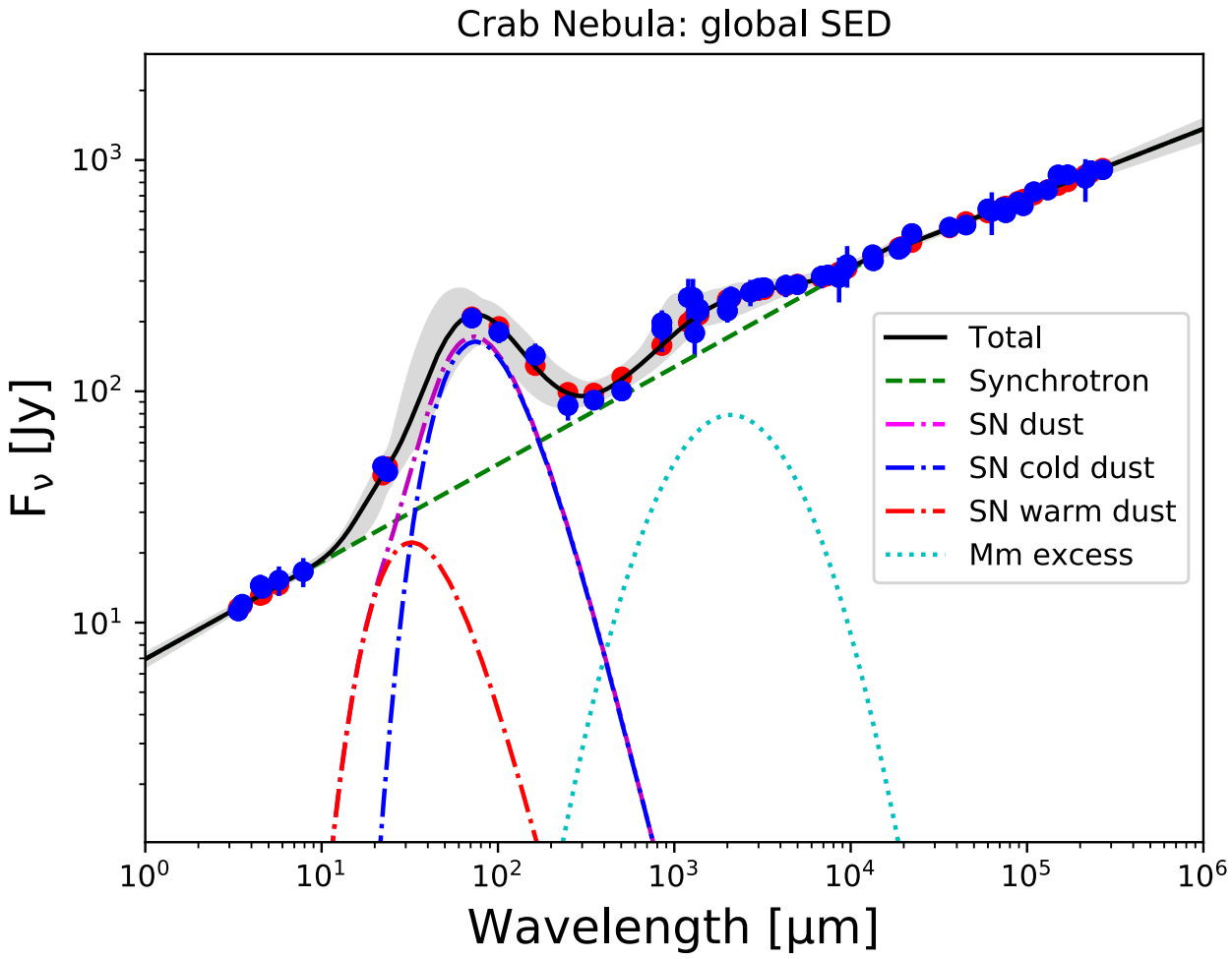

Figure 3. Total integrated SED for the Crab Nebula extending from near-infrared to radio wavebands. The best-fitting SED model is indicated with a black solid line, with the grey shaded region corresponding to the 16th and 84th percentiles of the *N*-dimensional likelihood (i.e. corresponding to the 1σ upper and lower bounds to the model). The blue dots correspond to the observed datapoints (with the uncertainties shown as vertical lines), while the red circles indicate the model flux densities in those wavebands. We have also included the emission of individual model components: synchrotron radiation (green dashed curve), mm excess emission (blue dashed curve), cold and warm SN dust SEDs (blue and red dot–dashed curves, respectively), and the combined SN dust emission (purple dot–dashed curve).

fitting results to fix the value for $\alpha_{\rm radio} = 0.297$, which corresponds to the median likelihood value inferred from the total integrated fit (see Table 5), and is independent of the assumed SN dust grain species. This fixed value for $\alpha_{\rm radio}$ is justified based on the spatially uniform radio spectral index map inferred by Bietenholz et al. (1997) on resolved scales.

Due to the computational cost of SED modelling on a pixel-by-pixel basis, we only performed the modelling for a single SN dust species. Based on the best-fitting models to the total integrated flux densities (see Table 4), and the large fractional carbon abundance in the gas phase in the Crab, we have opted for amorphous carbon 'a-C' grains with radii $a = 1$ μm, which rely on the optical constants inferred from recent laboratory studies, from Jones (2012a,b,c).[10] The total integrated fitting results suggest that the SN dust emission is dominated by a single-temperature component with a well characterized dust temperature, while the dust temperature of the other component is poorly constrained. Since the total integrated fits for carbonaceous grains tend to be dominated by cold (∼43–50 K) dust, we fix the warm dust temperature $T_{\rm warm} = 70$ K in the resolved models. The prior range for the break wavelength was extended from 10 μm to 60 mm for the resolved modelling procedure. Figs 5 and F2 show a representative Bayesian SED model, and corresponding 1D and 2D posterior distributions inferred for a central pixel in the Crab Nebula, respectively.

Resolved maps of the synchrotron spectral index, 1.4 GHz synchrotron flux density, SN dust temperatures and masses are presented in Fig. 6. We will now discuss the total integrated and resolved modelling results related to the Crab's synchrotron radiation (Section 5), supernova dust emission (Section 6), and millimetre excess emission (Section 7).

[10] Although the best fit was obtained for $Mg_{0.7}SiO_{2.7}$ grains, the total dust mass required to fit the total integrated emission of the Crab (by far) exceeds the maximum dust mass expected to condense out of the available metals. The lack of any dust continuum features in the *Spitzer* spectra furthermore rules out a dominant silicate dust population in the Crab.

5 THE CRAB'S SYNCHROTRON RADIATION

The most probable value of the integrated synchrotron spectral index in the radio wavelength domain is peaked around $\alpha_{\rm radio} =$

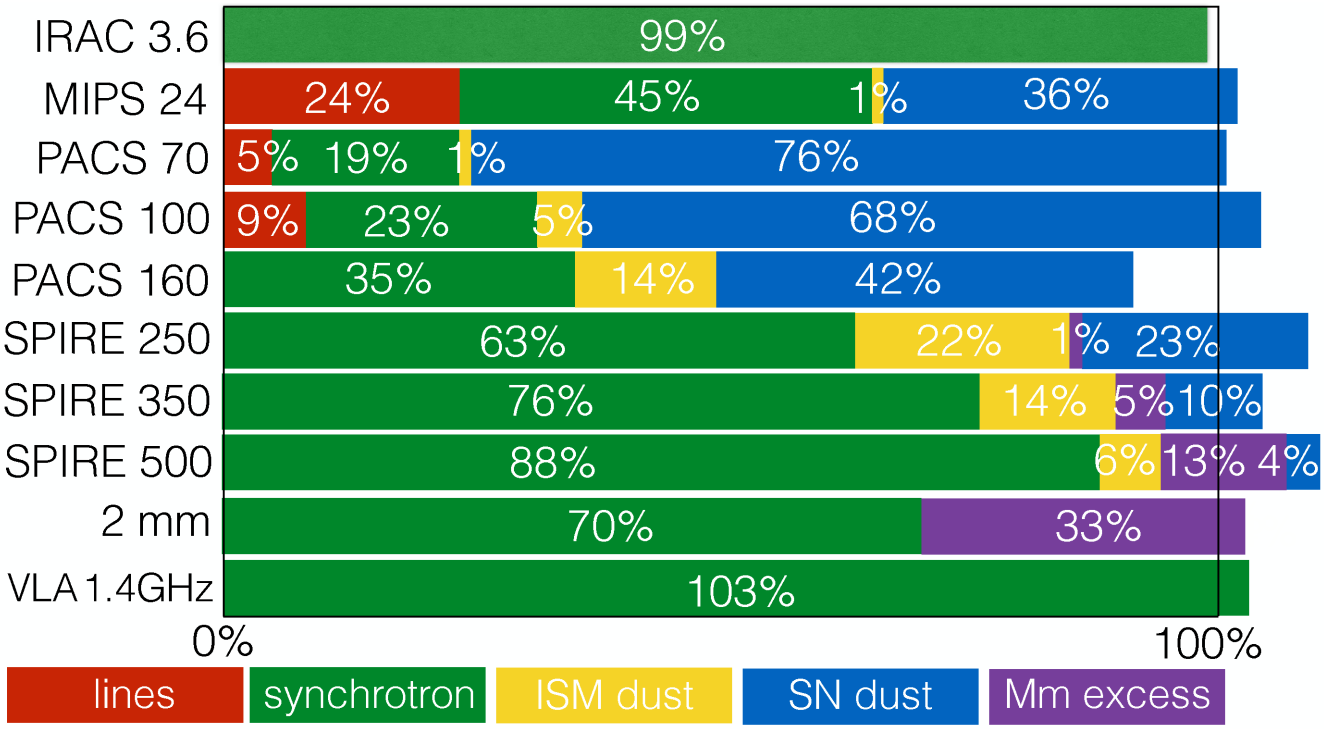

Figure 4. Overview of the contributions of different components (line emission, synchrotron radiation, ISM dust emission, mm excess, and SN dust emission) to the observed flux densities in each waveband, as inferred from the total integrated best-fitting SED model assuming amorphous carbon 'a-C' grains for the SN dust component. The graph shows the results for a selected number of representative wavebands; the individual contributions for omitted wavebands can be retrieved from Table 3. The ISM dust contributions were inferred as described in Appendix C. Because the Bayesian model is fitting the observed flux densities within the limits of uncertainty, the fractional contributions do not always exactly add up to a 100 per cent.

0.297 (see Fig. F1), consistent with the index of $\alpha = 0.3$ derived about 40 yr ago by Baars et al. (1977) and the radio spectral index $\alpha = 0.299$ inferred by Gomez et al. (2012). The posterior distribution for the IR spectral index peaks around $\alpha_{\rm IR} = 0.42$, which resembles the value $\alpha = 0.417$ inferred by Gomez et al. (2012). However, the wide tail in the 1D posterior distribution extending towards $\alpha_{\rm IR} = 0.46$ suggests that a steeper slope cannot be ruled out by the data. In fact, the parameter value for $\alpha_{\rm IR}$ strongly depends on the position of the synchrotron break: the IR spectral index is shallower ($\alpha_{\rm IR} = 0.42$) for a break at longer wavelengths ($\lambda_{\rm break} \sim$17 mm); while a steeper slope ($\alpha_{\rm IR} = 0.45$) is required for a short wavelength break ($\lambda_{\rm break} \sim$ 4 mm). Other than for $\alpha_{\rm IR}$ and $\lambda_{\rm break}$, a hint of a bimodality is also seen in the 1D posterior distribution of the peak millimetre emission, $F_{\rm mm,\,peak}$ (see Section 7). There is a degeneracy between the contribution of mm excess emission to the total integrated SED, the wavelength of the break in the synchrotron spectrum and the IR spectral index, which cannot be disentangled based on our current set of observations. However, the highest probability (by far) of the Bayesian model is given to the model solution with a synchrotron spectral break around 17 mm, an IR spectral index $\alpha_{\rm IR} \sim 0.42$ and a strong excess peaked around 150 GHz (or 2 mm), regardless of the assumed SN dust species. The model synchrotron emission at 1.4 GHz is peaked around ∼860 Jy, which corresponds well with the observed flux density (within the error bars) at the same frequency (see Table 3).

In our resolved SED models, the infrared spectral index $\alpha_{\rm IR}$ varies from 0.36 in the inner regions up to 0.58 in the outer regions (see Fig. 6, top right panel); these spatial variations are significant with respect to the average model uncertainties (<0.01) on these $\alpha_{\rm IR}$ values. The average luminosity-weighted IR index ($\alpha_{\rm IR} = 0.433$) is consistent with the total integrated value ($\alpha_{\rm IR} = 0.429$) for the Crab (see Table 5). The IR spectral index is flatter in the inner regions, in particular around the torus and jet structures, and steepens in the outer regions, which is consistent with the spectral index map derived based on optical and near-infrared images (Veron-Cetty & Woltjer 1993; Temim et al. 2012; Lyutikov et al. 2018). This steepening of the spectrum towards the outer regions has been interpreted in terms of a scenario in which electrons emitting at optical and near-infrared wavelengths have fast cooling times, shorter than the age of the Crab itself (e.g. Kennel & Coroniti 1984; Atoyan & Aharonian 1996; Bandiera et al. 2002; Meyer, Horns & Zechlin 2010; Schweizer et al. 2013; Porth, Komissarov & Keppens 2014a; Lyutikov et al. 2018). We show in this paper that this trend continues into the FIR and (sub-)millimeter wavelength regime, and that radiative losses also affect these longer wavelengths. The average IR spectral index at the position of the Crab's torus and the jet is close to 0.36, and thus somewhat steeper than the average radio spectral index of 0.297. According to our models, the infrared and (sub-)millimetre regime correspond to a fast cooling regime, while the radio synchrotron spectrum is dominated by a slow cooling regime. These differences between the central radio and infrared spectral index, and radial variations inferred for the infrared spectral index suggest the presence of two mechanisms responsible for the acceleration of these particles (Bandiera et al. 2002; Lyutikov et al. 2018).

We have also attempted to constrain the position of the synchrotron break on resolved scales (see Fig. 6, top left panel). Although the range of possible 'break' wavelengths is rather wide (see Fig. F2), we observe a clear dichotomy between the inner and

Table 4. Overview of the median likelihood dust parameters inferred from a Bayesian SED modelling procedure on total integrated (top part) and resolved (bottom part) scales for a variety of distinct models assuming a single grain species. The model parameters describing the Crab's synchrotron radiation and mm excess emission are detailed in Table 5. Column 1 presents the different dust species and corresponding references (in superscript) from which their dust optical constants were adopted: (a) Rouleau & Martin (1991), (b) Jones (2012a,b,c) for a-C grains with a band gap $E_g = 0.1$ eV, (c) Dorschner et al. (1995), (d) Jäger et al. (2003), (e) Takashi Nozawa and Eli Dwek (private communication). We adopted mass densities of 1.6 g cm^{-3} for amorphous carbon grains, 2.5 g cm^{-3} for silicate-type grains (Jones et al. 2013), and 7.89 g cm^{-3} for iron grains (Nozawa, Kozasa & Habe 2006). The reduced χ^2 values inferred from all near-infrared to radio observational constraints, and the dust-only χ^2_{red} (calculated for WISE 22 to SPIRE 500 μm wavebands, which have non-negligible supernova dust contributions) are reported in Columns 2 and 3, respectively. Columns 4–7 report the temperatures and masses for warm and cold supernova dust components. The total (warm + cold) dust masses are summarized in Column 8 (assuming a distance to the Crab of $D = 2$ kpc). These dust masses could go up by a factor of 2.8 based on the revised distance estimate for the Crab inferred from *Gaia* data (Fraser & Boubert 2019). The maximum expected dust masses for different grain species are provided in Column 9 based on a condensation efficiency of 100 per cent and the estimated yields from nucleosynthesis models from Woosley & Weaver (1995) for a progenitor mass of 11 M$_\odot$. The resolved model parameters correspond to the median dust temperatures calculated over all modelled pixels, while the dust masses correspond to the sum of the model dust masses over all pixels. The results obtained for our preferred grain model (a-C $a = 1$ μm grains) are indicated in boldface.

Parameters:			Warm dust		Cold dust		Total dust	100 per cent cond. eff.
(1)	(2)	(3)	(4)	(5)	(6)	(7)	(8)	(9)
			T_{warm} [K]	log M_{warm} [log M$_\odot$]	T_{cold} [K]	log M_{cold} [log M$_\odot$]	M_{total} [M$_\odot$]	M_{max} [M$_\odot$]
			Total integrated SED fitting					
Dust species:	χ^2_{red}	χ^2_{red}(dust)						
Zubko 'ACAR' [a]	1.9	1.3	69^{+21}_{-12}	$-3.44^{+1.43}_{-1.70}$	48^{+8}_{-14}	$-1.89^{+0.30}_{-0.44}$	$0.013^{+0.022}_{-0.009}$	0.054
Zubko 'BE' [a]	1.9	1.0	72^{+20}_{-17}	$-3.44^{+1.48}_{-1.02}$	43^{+9}_{-9}	$-1.61^{+0.32}_{-0.28}$	$0.025^{+0.037}_{-0.012}$	0.054
Am. carbon 'AC1' [a]	1.9	1.4	65^{+22}_{-4}	$-2.30^{+0.41}_{-1.90}$	50^{+9}_{-22}	$-1.88^{+0.18}_{-1.24}$	$0.018^{+0.015}_{-0.017}$	0.054
Am. carbon 'BE1' [a]	1.9	1.6	68^{+21}_{-11}	$-3.26^{+1.22}_{-1.77}$	48^{+9}_{-17}	$-1.94^{+0.31}_{-0.68}$	$0.012^{+0.021}_{-0.010}$	0.054
a-C $a = 0.1$ μm[b]	1.9	1.3	69^{+21}_{-10}	$-3.13^{+1.22}_{-1.78}$	49^{+9}_{-17}	$-1.83^{+0.29}_{-0.61}$	$0.016^{+0.026}_{-0.012}$	0.054
a-C $a = 1$ μm[b]	**1.9**	**1.2**	$\mathbf{69^{+21}_{-12}}$	$\mathbf{-3.34^{+1.45}_{-1.93}}$	$\mathbf{50^{+7}_{-14}}$	$\mathbf{-1.80^{+0.26}_{-0.51}}$	$\mathbf{0.016^{+0.026}_{-0.011}}$	**0.054**
a-C $a = 1$ μm, ev. synchr.[b]	2.3	8.2	66^{+22}_{-10}	$-3.59^{+1.70}_{-2.18}$	53^{+4}_{-18}	$-1.86^{+0.14}_{-0.88}$	$0.014^{+0.018}_{-0.012}$	0.054
$MgSiO_3$[c]	2.1	3.4	79^{+3}_{-3}	$-1.93^{+0.06}_{-0.08}$	35^{+19}_{-17}	$-3.06^{+0.79}_{-0.65}$	$0.013^{+0.006}_{-0.003}$	0.050
$Mg_{0.7}SiO_{2.7}$[d]	1.9	0.9	61^{+25}_{-18}	$-2.90^{+2.55}_{-1.12}$	38^{+4}_{-6}	$-0.07^{+0.26}_{-0.19}$	$0.85^{+1.14}_{-0.30}$	0.063
Fe $a = 0.1$ μm[e]	2.1	3.4	79^{+3}_{-3}	$-0.67^{+0.07}_{-0.11}$	37^{+19}_{-18}	$-2.34^{+1.34}_{-1.10}$	$0.22^{+0.13}_{-0.05}$	0.105
Fe $a = 1$ μm[e]	2.1	3.2	79^{+3}_{-3}	$0.48^{+0.06}_{-0.08}$	35^{+19}_{-16}	$-0.87^{+0.86}_{-0.77}$	$3.14^{+1.32}_{-0.63}$	0.105
			Resolved SED fitting					
a-C $a = 1$ μm[b]	–	–	70 (fixed)	$-2.77^{+0.06}_{-0.07}$	41^{+3}_{-2}	$-1.42^{+0.09}_{-0.09}$	$0.039^{+0.010}_{-0.007}$	0.054

outer regions of the Crab Nebula. The inner regions correspond to a break occurring at longer wavelengths (20–30 mm), while the break occurs at shorter wavelengths (2–4 mm) in the outer Crab regions. These two regimes are also reflected in the bi-modality of the break wavelength in the total integrated SED (see Fig. F1), where a high likelihood was attributed to a synchrotron break at cm wavelengths (as observed in the emission-dominating inner regions). This scenario is consistent with the cm and longer wavelength radio wavelengths being significantly affected by synchrotron losses in the central Crab regions, while the outer regions are also prone to synchrotron losses at shorter wavelengths. Similar inferences were made by Bandiera et al. (2002), who derived a longer wavelength break in dense filaments, and interpreted it in terms of the presence of stronger magnetic fields.

It is important to note that the absolute wavelengths inferred for the position of the break will sensitively depend on the assumed synchrotron model (i.e. a broken-power law or evolutionary break model). Earlier studies demonstrated that a spectral break occurs around 20 μm in the integrated spectrum of the Crab Nebula, consistent with estimates of the average Crab's magnetic field B of 200 μG (Bucciantini, Arons & Amato 2011). The best-fitting model for an evolutionary synchrotron spectrum (see Appendix E) similarly suggests a break in the spectrum around 24 μm, in line with previous estimates. Due to the sensitivity of the break position to the assumed synchrotron model, we focus the discussion here on the relative differences observed in our resolved synchrotron spectral break map.

The synchrotron brightness at 1.4 GHz (see Fig. 6, top-right panel) peaks near the pulsar and the toroidal structures around the pulsar (see Fig. 1 for comparison), with an extension towards the north and north-west of the PWN, similar to the morphology of radio emission observed for the Crab Nebula (e.g. Bietenholz et al. 2015). The sum over all modelled pixels at 1.4 GHz (725^{+45}_{-47} Jy, see Table 5) is consistent with the summed emission in the observed 1.4 GHz image (675 ± 135 Jy). Note that the sum of the resolved flux densities is lower than the total integrated flux density at 1.4 GHz (834 ± 175 Jy, see Table 3) due to the total integrated measurement encompassing a larger aperture than the resolved pixel-by-pixel analysis (which required pixels to attain a certain signal to noise).

It is important to note that re-running the models on resolved scales with the inclusion of the 1.3, 2, and 3.3 mm data, we were unable to simultaneously fit the FIR/submm *Herschel* and mm observations in the central regions of the SNR, as these models would significantly overestimate the SPIRE fluxes with a synchrotron

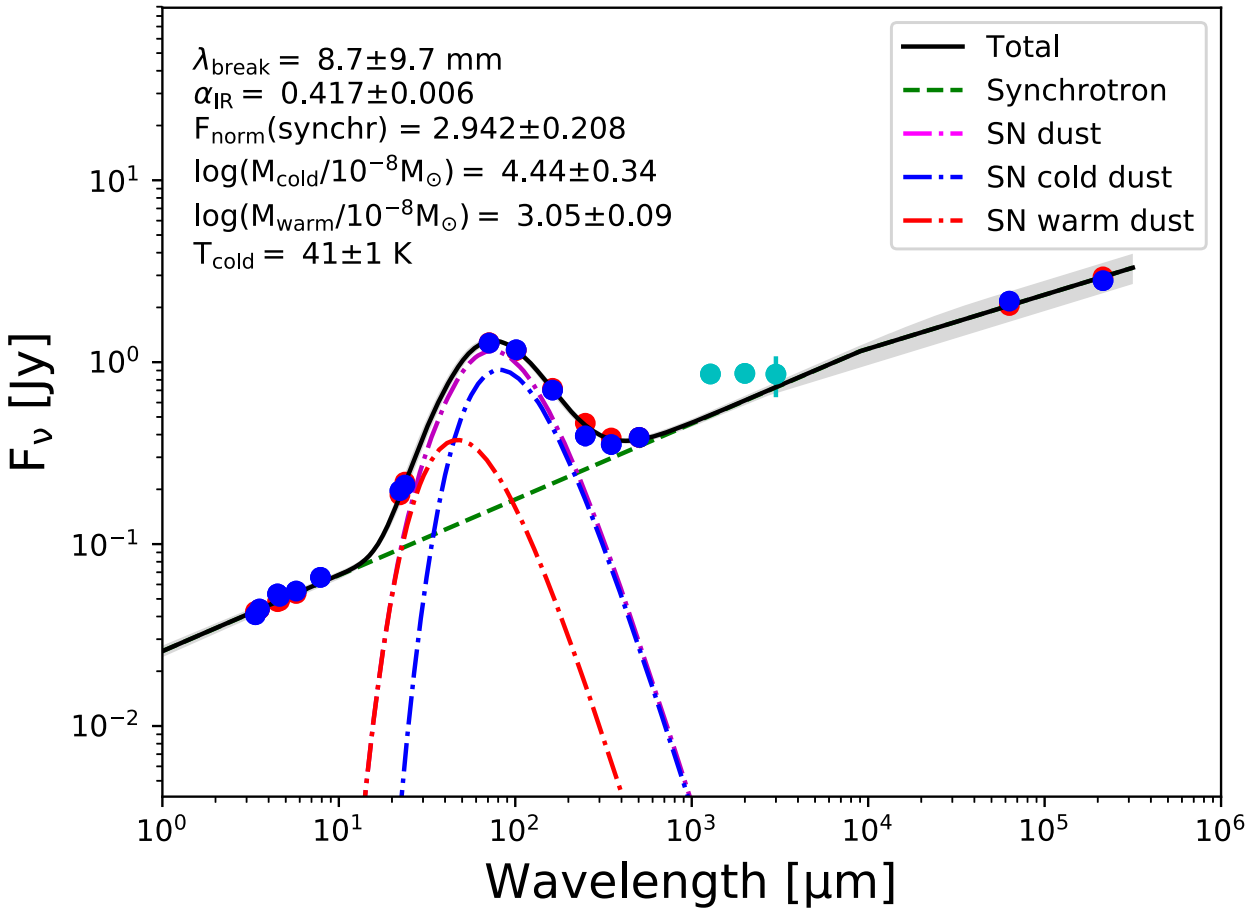

Figure 5. Representative example of a resolved SED fit for a central pixel in the Crab Nebula. The best-fitting SED model is indicated with a black solid line, with the grey shaded region corresponding to the 16th and 84th percentiles of the *N*-dimensional likelihood (i.e. corresponding to the 1σ upper and lower bounds to the model). We have also included the emission of individual model components: synchrotron radiation (green dashed curve), cold and warm SN dust SEDs (purple dot–dashed curves), and the combined SN dust emission (cyan dot–dashed curve). The best-fitting model parameters (maximum-likelihood and standard deviation) of each of the parameters are summarized in the top left corner of the plot. The blue dots correspond to the observed datapoints (with the uncertainties shown as vertical lines), while the red circles indicate the model flux densities in those wavebands. The cyan dots correspond to the mm flux densities in those pixels, which are shown for comparison, as these were not used to constrain the models.

spectrum constrained by the IRAC and *WISE* near-infrared fluxes and mm data points, and thus seem to require the addition of a mm excess component in the model. It can however not be ruled out that models including spatial variations in the spectral break, multiple spectral breaks, and/or multiple synchrotron components would be able to remedy this situation. In Section 7 and Appendix D, we will discuss these and other alternative scenarios, respectively, to account for the mm excess observed in the Crab Nebula.

Overall, the excellent agreement between the spectral indices and the spatial variations within the remnant derived by Temim et al. (2012) and in this paper, makes us confident that our model is appropriate to reproduce the Crab's synchrotron radiation in the IR wavelength domain, and demonstrates the need for a spatially resolved synchrotron model to infer the residual emission that can be attributed to SN dust (see Section 6).

6 SUPERNOVA DUST EMISSION AND EXTINCTION

The SN dust emission in the total integrated SED of the Crab was modelled using a combination of warm and cold SN dust temperature components. Table 4 presents the warm and cold dust masses and temperatures, and combined dust masses for a range of different grain species inferred from the same modelling technique. The best dust SED fits (with the lowest reduced χ^2_{dust} values) were obtained for amorphous carbon grains ('AC1', 'BE1', 'ACAR', 'BE', and 'a-C') and silicate-type grains with low Mg-to-O ratios ($Mg_{0.7}SiO_{2.7}$). The model fits deteriorate for Mg protosilicates ($MgSiO_3$) and iron grains (with sizes $a = 0.1$ and $a = 1$ μm) due to an overprediction of the observed SPIRE fluxes by the model.

The posterior distributions (see Fig. F1) demonstrate that the SN dust SED is dominated by a well-constrained single-temperature (warm or cold) component, while the posterior distribution for the dust temperature of the other component (with minimal contribution to the overall SN dust emission) tends to be flat. Although a better fit is still obtained using a two-component MBB model, reasonably good fits can thus be obtained with a single-T_{dust} component. The cold dust temperature in the model ranges from 38^{+4}_{-6} K (for $Mg_{0.7}SiO_{2.7}$ grains) to 48^{+9}_{-17}, 50^{+9}_{-22}, 48^{+8}_{-14}, 43^{+9}_{-9}, and 50^{+7}_{-14} K (for amorphous carbon 'BE1', 'AC1', 'ACAR', 'BE', and 'a-C' grains, respectively). These dust temperatures are high compared to the average cold dust temperatures inferred by Gomez et al. (2012) for silicates ($T_{d,\,cold} = 28^{+6}_{-3}$ K) and amorphous carbon 'BE' grains ($T_{d,\,cold} = 34^{+2}_{-2}$ K), but somewhat more similar to their one-

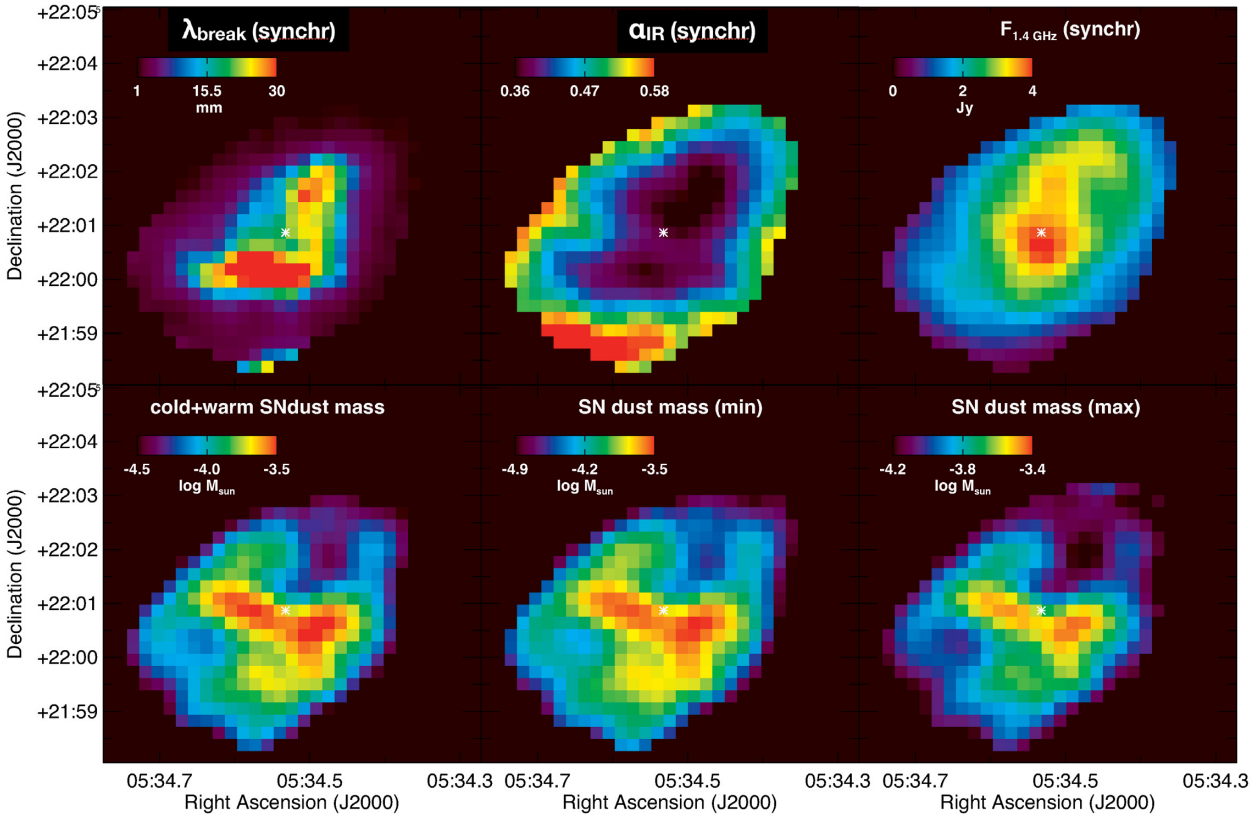

Figure 6. Resolved maps of the modelled wavelength break, λ_{break} (top row, left), IR spectral index, α_{IR} (top row, middle), 1.4 GHz synchrotron flux density (top row, right), total SN dust mass per pixel (bottom row, left), and lower and upper limits on the SN dust mass per pixel (bottom row, middle, and right, respectively), as inferred from a Bayesian SED fitting algorithm on resolved scales of 14 × 14 arcsec^2 (or 0.136^2 pc^2, for a distance of 2 kpc).

Table 5. Overview of the median likelihood parameters describing the Crab's synchrotron radiation and mm excess emission as inferred from a Bayesian SED modelling procedure on total integrated (top part) and resolved (bottom part) scales for amorphous carbon 'a-C' grains. The model parameters for other Bayesian models (assuming different supernova grain species) were omitted due to the independence of the synchrotron and mm excess model parameters on the SN grain model. Columns 2–5 present the synchrotron model parameters inferred for the radio spectral index, α_{radio}, infrared spectral index, α_{IR}, wavelength of the spectral break, λ_{break}, and the synchrotron flux density, $F_{1.4\,GHz}$, respectively. The peak frequency, ν_{peak}, the peak flux density, $F_{mm,\,peak}$, and width, σ, of the spectrum describing the mm excess emission are presented in Columns 6–8, respectively. The resolved model parameters correspond to the luminosity-weighted values, while the flux density $F_{1.4\,GHz}$ corresponds to the sum of the synchrotron model flux densities over all pixels.

Parameters:		Synchrotron			Excess emission		
(1)	(2)	(3)	(4)	(5)	(6)	(7)	(8)
Dust species:	α_{radio}	α_{IR}	λ_{break} [mm]	$F_{1.4\,GHz}$ [Jy]	ν_{peak} [GHz]	$F_{mm,\,peak}$ [Jy]	Width σ
Total integrated SED fitting							
a-C a = 1 μm	$0.297^{+0.009}_{-0.009}$	$0.429^{+0.021}_{-0.009}$	$9.0^{+8.4}_{-5.1}$	862^{+17}_{-16}	163^{+42}_{-22}	69^{+14}_{-23}	$0.27^{+0.06}_{-0.08}$
a-C a = 1 μm, ev. synchr.	$0.359^{+0.016}_{-0.049}$	–	$1.1^{+8.3}_{-1.0}$	921^{+20}_{-25}	68^{+43}_{-21}	69^{+12}_{-21}	$0.62^{+0.15}_{-0.30}$
Resolved SED fitting							
a-C a = 1 μm	0.297 [fixed]	$0.433^{+0.007}_{-0.007}$	$11.5^{+2.9}_{-1.7}$	725^{+45}_{-47}	–	–	–

component fits for silicates (T_{dust} = 34 K) and carbonaceous 'BE' grains (T_{dust} = 40 K). Our inferred dust temperature is also in agreement with the dust temperature (T_{dust} = 42.1 ± 1.1 K) inferred by Nehmé et al. (2019), and with the dust temperatures T_{dust} = 45 K (for silicates) and T_{dust} = 45 K (for graphite grains) inferred by Green et al. (2004). Models dominated by a warm component have dust temperatures $T_{warm} = 79^{+3}_{-3}$ K (for iron grains), which are higher than the warm dust temperatures for silicate ($T_{warm} = 56^{+8}_{-3}$ K) and carbon ($T_{warm} = 63^{+5}_{-3}$ K) grains from Gomez et al. (2012).

The total (cold + warm) supernova dust masses required to reproduce the Crab's total integrated infrared dust SED vary significantly from one grain species to another. Average carbon dust masses of $0.018^{+0.015}_{-0.017}$ $M_\odot$ ('AC1' grains), $0.012^{+0.021}_{-0.010}$ $M_\odot$ ('BE1' grains), $0.013^{+0.022}_{-0.009}$ $M_\odot$ ('ACAR' grains), $0.025^{+0.037}_{-0.012}$ $M_\odot$ ('BE' grains), and $0.016^{+0.026}_{-0.011}$ $M_\odot$ ('a-C' grains) are required to fit the infrared SED, which are all consistent within the error bars regardless of the assumed carbon dust emissivities (see Fig. 2). These inferred dust masses are within the limits of the amount of carbon produced in

the progenitor star (0.054 $M_\odot$). Models for supernova dust with an iron composition would require $0.22^{+0.13}_{-0.05}$ $M_\odot$ (a = 0.1 μm) or $3.14^{+1.32}_{-0.63}$ $M_\odot$ (a = 1 μm) of dust to reproduce the emission, which greatly exceeds the maximum amount of iron expected to be present (0.105 $M_\odot$[11]). Similarly, we would require $0.85^{+1.14}_{-0.30}$ $M_\odot$ of $Mg_{0.7}SiO_{2.7}$ grains to fit the supernova dust emission, which is at least an order of magnitude higher than the available metal content for grain condensation (0.063 $M_\odot$). On the other hand, a reasonable mass ($0.013^{+0.006}_{-0.003}$ $M_\odot$) of $MgSiO_3$ grains suffices to fit the SED. The nearly two orders of magnitude difference in dust masses inferred for these silicate-type dust species results from the lower FIR/submm dust emissivities (by a factor of 10) of $Mg_{0.7}SiO_{2.7}$ grains compared to $MgSiO_3$ (see Fig. 2). In addition, the Bayesian model reproduces most of the Crab's dust emission using warm (79 K) $MgSiO_3$ grains, while 38 K $Mg_{0.7}SiO_{2.7}$ grains are preferred.

Based on nucleosynthesis arguments, we can rule out that iron (a = 0.1 or 1 μm) or $Mg_{0.7}SiO_{2.7}$ grains dominate the supernova dust emission in the Crab Nebula. The nearly featureless dust continuum in *Spitzer* IRS spectra (Temim et al. 2012) is also consistent with the absence of a significant mass of $Mg_{0.7}SiO_{2.7}$ (or any other silicate-type) grains. We can however not rule out that some iron (<0.105 $M_\odot$) and $Mg_{0.7}SiO_{2.7}$ (<0.063 $M_\odot$) grains have formed in the Crab Nebula. While warm $Mg_{0.7}SiO_{2.7}$ dust has been detected in several Galactic SNRs (Cas A, G54.1; Rho et al. 2008; Temim et al. 2017), we inferred that it is impossible for these silicate-type grains to be responsible for most of the (cold) dust mass in SNRs (at least for the Crab and Cassiopeia A, see De Looze et al. 2017 for the latter) due to their low-grain emissivities at submm wavelengths (see Fig. 2).

We assumed a grain size of 1 μm for most dust species explored in this model, based on a series of recent (independent) studies consistent with large (>0.1 μm) dust grains growing in SNRs at late times (e.g. Gall et al. 2014; Owen & Barlow 2015; Wesson et al. 2015; Bevan & Barlow 2016, Priestley, Barlow & De Looze 2019). For most grain species, our grain size assumption will not affect the inferred dust masses due to the weak dependence of the dust mass absorption coefficient, κ_{abs}, at infrared and submm wavelengths long wards of the typical grain radii (i.e. >1 μm). We tested this assumption for a-C grains with radii a = 0.1 and 1 μm; no significant differences in the inferred SN dust model parameters were inferred (see Table 4). However, iron grains form an exception with a = 1 μm grains being up to ten times more emissive at submm wavelengths compared to a = 0.1 μm grains (Nozawa et al. 2006; see Fig. 2), which has an impact on the inferred iron dust masses for different grain sizes (see Table 4).

Based on earlier *Herschel* studies, our dust mass estimates are up to an order of magnitude lower than dust mass predictions from Gomez et al. (2012) (M_{dust} = $0.24^{+0.32}_{-0.08}$ $M_\odot$ for silicates and M_{dust} = 0.11 ± 0.01 $M_\odot$ for amorphous carbon 'BE' grains), and from Owen & Barlow (2015) (M_{dust} = 0.18–0.27 $M_\odot$ for clumps of carbon grains), but overlap with the estimated dust mass range from Temim & Dwek (2013) (0.016–0.061 $M_\odot$, for amorphous carbon 'AC' grains) and Nehmé et al. (2019) (M_{dust} = 0.056 ± 0.037 $M_\odot$, assuming a single MBB body function with dust emissivity index β = 1.5 and dust mass absorption coefficient $\kappa_{100\,\mu m}$ = 40 cm^2 g^{-1}). The supernova dust masses inferred by Priestley et al. (in preparation) from modelling our supernova dust SED (see Table 3) with amorphous carbon 'ACAR' (0.026–0.039 $M_\odot$) and 'BE' (0.032–0.076 $M_\odot$) grains,[12] allowing the grain size distribution to vary, heated by the PWN radiation field and by collisions with electrons and ions in the ambient gas, fall within the range of values reported in this paper for the same type of grains. Only for $MgSiO_3$ (0.076–0.218 $M_\odot$ silicate grains do their supernova dust masses tend to be significantly higher compared to ours due to their lower inferred dust temperatures (T_{dust} = 25 K) for 1 μm-sized grains. Temim & Dwek (2013) attributed their lower dust masses mainly to the use of more emissive carbon grains. However, their large error bars on observed SPIRE 350 and 500 μm data points made it hard to accurately constrain the Crab's dust mass. Instead, we argue that our lower dust masses can mostly be attributed to our different correction for ISM dust emission (see Appendix C), which has resulted in lower SPIRE 350 and 500 μm 'supernova dust' fluxes (see Table 3). These lower submm fluxes have resulted in the derivation of higher dust temperatures and thus lower dust masses, for a diverse set of grain species characterized by different dust optical constants, compared to estimates reported in previous papers.

Summing the dust masses from each pixel, we infer a dust mass of $0.039^{+0.010}_{-0.007}$ $M_\odot$ for amorphous carbon 'a-C' grains. The cold dust component accounts for most mass ($0.038^{+0.009}_{-0.007}$ $M_\odot$) and has an average dust temperature of 41^{+3}_{-2} K. The warm dust component (with a warm dust temperature fixed at 70 K) accounts for $0.0017^{+0.0003}_{-0.0003}$ $M_\odot$ of mass. Our resolved supernova dust mass of 0.032–0.049 $M_\odot$ (for amorphous carbon 'a-C' grains with size a = 1 μm) spans a smaller range of possible values compared to the dust mass inferred from the total integrated flux densities for the same grain species (0.005–0.042 $M_\odot$), which we argue can be attributed to an accurate modelling of spatial variations in the synchrotron spectrum and the supernova dust temperature and mass distribution on resolved scales, which was averaged over for the total integrated SED fits. Compared to the heavy element mass predicted by nucleosynthesis models (0.42 $M_\odot$, for a 11 $M_\odot$ progenitor star, Woosley & Weaver 1995), the modelled dust masses for 'a-C' grains correspond to a dust condensation efficiency of 8–12 per cent. The inferred dust condensation efficiency is consistent with estimates of the dust condensation efficiency for Cassiopeia A (0.1–0.17, Nozawa et al. 2010; Raymond et al. 2018; Priestley et al. 2019).

In our resolved model, most supernova dust is located south of the pulsar (see Fig. 6, bottom left-hand panel), coincident with the dense filaments of thermally excited ejecta observed in the optical and IR (see Fig. 1; Davidson 1979; Graham et al. 1990; Blair et al. 1992), and with the detection of dense knots of molecular gas (Graham et al. 1990; Loh, Baldwin & Ferland 2010; Loh et al. 2011, 2012). The overall dust mass distribution peaks at the locations of dense thermal filaments, and shows a deficit towards the north-west of the remnant. The dust mass in the north-west part of the remnant may be lower due to the lack of sufficiently dense filaments where elements could have more easily accreted on to grain seeds and grown dust. The absence of a dense circum- or ISM has resulted in higher shock velocities towards the NW (Lawrence et al. 1995) and has prevented the gas from cooling sufficiently after passage of the shock, with cooling time-scales longer than the age of the Crab Nebula (Sankrit & Hester 1997; Hester 2008), and may provide an explanation for the lower supernova dust masses towards the NW. The most prominent Crab's filaments are thought

[11]The estimated iron grain mass from nucleosynthesis models (Woosley & Weaver 1995) accounts for the amount of iron produced by the star, but also the formation route of iron through radiative decay of nickel.

[12]The uncertainties on their supernova dust mass measurements are driven by the assumed distance to the heating sources.

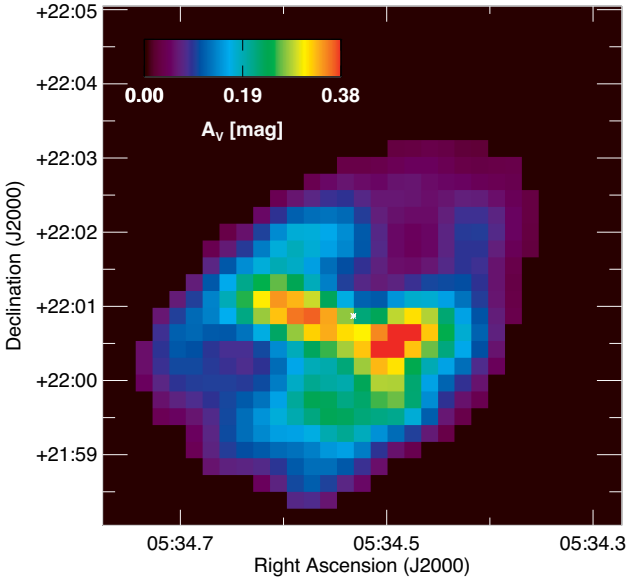

Figure 7. Map of the *V*-band extinction (A_V, right) along the line of sight to the Crab Nebula, as inferred from the cold + warm supernova dust mass (see Fig. 6, bottom right-hand panel). The white cross indicates the position of the Crab pulsar.

to have formed through Rayleigh–Taylor instabilities about 100–200 yr after the explosion (Jun 1998; Porth, Komissarov & Keppens 2014b), implying that the dust was only later assembled in these filaments as the onset of dust formation is thought to take place 300–500 d after explosion with the build up of dust mass lasting several tens of years (Gall et al. 2014; Wesson et al. 2015; Bevan & Barlow 2016). It is of interest that dust is not only present in dense filaments but appears to be distributed throughout the remnant, which presumably indicates that dust is present in smaller filaments or globules, as observed by e.g. Grenman et al. (2017), which remain unresolved by our infrared observations.

We converted our resolved supernova dust mass map to a measure of the *V*-band extinction, A_V (see Fig. 7), for which we relied on the A_V-to-dust column density ratio inferred for 'a-C' grains. The highest values ($A_V = 0.20$–0.39 mag) correspond to the dense filaments, while A_V ranges between 0.05 and 0.10 mag in most parts of the nebulae. The lowest $A_V = 0.05$ mag values are inferred for the outskirts of the Crab. Our *V*-band extinction estimates ($A_V = 0.20$–0.39 mag) in the dense filaments are in excellent agreement with the *V*-band extinction ($A_V = 0.20$–0.34 mag) measured directly from optical images by Grenman et al. (2017) for seven dark and distinct globules, and makes us confident that our inferred dust masses are accurate. We should note that the median A_V (0.10 ± 0.08 mag) along the line of sight to the Crab is significantly lower than the A_V (1.08 ± 0.39 mag) inferred from the IS dust emission in the vicinity of the nebula, which suggests that there is about an order of magnitude more IS extinction along the line of sight to the Crab compared to supernova dust. None the less, the emission in the FIR wavebands is dominated by thermal emission from supernova dust, and the contributions from IS and supernova dust emission are comparable at submm wavelengths, because the average supernova dust temperature ($T_{\rm dust} = 41$ K) is significantly higher than the median ISM value ($T_{\rm dust} = 15$ K, see Appendix C).

We conclude that the dust mass (0.032–$0.049\,{\rm M}_\odot$) formed in the Crab Nebula is consistent with a scenario of efficient dust condensation (8–12 per cent) in the supernova ejecta; this result confirms that dust grains can efficiently condense in the post-explosion ejecta of supernova. Based on an updated distance to the Crab pulsar inferred from GAIA data, the Galactic remnant may be located significantly further from the Sun (3.37 kpc, Fraser & Boubert 2019) than previously thought (2 kpc, Trimble 1968). At this distance, the Crab's dust mass would increase to 0.091–$0.138\,{\rm M}_\odot$ with a dust condensation efficiency of 22–33 per cent. Although the Crab's dust mass is lower than the average dust mass (0.1–$1\,{\rm M}_\odot$) per single supernova event required to account for the dust budgets observed in the Early Universe (Morgan & Edmunds 2003), we might not expect a supernova from a progenitor star with mass 8–$11\,{\rm M}_\odot$ to produce $1\,{\rm M}_\odot$ of dust (simply because only $0.42\,{\rm M}_\odot$ of metals are expected to be present in the post-explosion ejecta). Most dust will instead be produced by higher mass progenitors (e.g. Cas A, SN 1987A). The dust mass inferred for the Crab Nebula is lower than the ones inferred for other Galactic PWNe (Chawner et al. 2019). Due to the careful selection of dust structures correlated with the PWNe and the temperature components warmer than the average IS dust by Chawner et al. (2019), their dust mass estimated have effectively been corrected for the background IS dust emission, in a similar way as was done in De Looze et al. (2017) and in this work, and is thus unlikely to account for the difference in inferred dust masses. Instead, the dissimilar dust masses are thought to be caused by a combination of effects. First of all, due to a difference in assumed dust properties with $\kappa_{850\,\mu{\rm m}} = 0.7\,{\rm m}^2\,{\rm kg}^{-1}$ (assumed in Chawner et al. 2019), which is about a factor of 3 lower compared to the standard 'a-C' dust model used to infer the Crab's resolved dust mass. Secondly, the infrared images in Chawner et al. (2019) were not corrected for possible line contributions; but given that line emission tends to have the highest contributions to mid- and FIR wavebands, it is not clear whether the cold dust mass estimates would be effected much. Finally, it is likely that the three PWNe from Chawner et al. (2019) result from progenitors with a higher mass (than that of the Crab progenitor) for which we expect to find an elevated mass of condensed grains in accordance to their more massive reservoirs of metals. A consistent comparison of PWN dust masses would require an accurate knowledge of the supernova dust composition (and its variation with SN explosion energy and progenitor mass) in PWNe. The Crab's dust production does confirm that PWNe are efficient dust factories (e.g. Omand, Kashiyama & Murase 2019).

7 MILLIMETRE-EXCESS EMISSION

In our total integrated SED model, the observed mm excess emission in the Crab Nebula is best described by a spectrum with peaks around $\nu_{\rm peak} = 163^{+42}_{-22}$ GHz (or around 2 mm), with a width of $\sigma = 0.27^{+0.06}_{-0.08}$ and amplitude of $F_{\rm mm,\,peak} = 69^{+14}_{-23}$ Jy. The model parameters to describe the excess emission at mm wavebands hold regardless of the assumed dust species. We note that a model with a broken power-law synchrotron spectrum was not capable of reproducing the observed fluxes in the mm wavelength range without accounting for a mm excess in the model. A synchrotron model with an evolutionary break might reduce the need for a separate component to account for mm excess emission, but degrades the quality of the fits at submm wavelengths. We note that the excess emission, as fitted by our total integrated SED model, accounts for 33 per cent of the emission at 2 mm, and can therefore not be attributed to short-term variability in radio brightness due to instabilities within the nebular flow (which is thought to result in variations up to 10 per cent at most, Bietenholz et al. 2015). An excess at millimetre wavebands in the Crab has been identified before by

several other authors (Bandiera et al. 2002; Macías-Pérez et al. 2010). In Section 7.1, we address the spatially resolved distribution of the mm excess emission, while we expand on the possible origin of the excess emission in Section 7.2.

7.1 Spatial distribution of excess emission

We employ an interpolation for every pixel of the resolved Bayesian SED models (see Section 4) to predict the millimetre emission inferred by our combined synchrotron and supernova dust model. Fig. 8 compares the observed 1.3, 2, and 3.3 mm images (left column) with the model interpolations (middle column). The final column presents the residual after subtracting the model emission from the observed mm wave maps. The residual emission peaks in the centre, and appears to roughly follow the structure of the torus and the jet as seen in X-ray (Seward, Tucker & Fesen 2006; Madsen et al. 2015) and in radio images (Velusamy, Roshi & Venugopal 1992; Bietenholz et al. 2015; Dubner et al. 2017) of the Crab Nebula (see Fig. 1), which had also been remarked on by Bandiera et al. (2002).

7.2 Origin of the mm-excess emission

To explain the mm excess emission in the Crab Nebula, we explore four different scenarios: (1) spatial variations in the synchrotron spectrum and/or a secondary synchrotron component; (2) free–free emission from a hot plasma; (3) spinning dust grains; or (4) magnetic (Fe-bearing) grains. We believe a synchrotron origin for the mm-excess emission is most likely, and discuss this scenario in more detail below. The other possible scenarios are discussed and compared with the expected location of the mm excess emission as inferred from residuals after subtracting the best-fitting resolved synchrotron model from the observed mm images (see Section 7.1), in Appendix D.

(1) Spatial variations or multiple synchrotron components: While the mm excess emission could not be reproduced with a single broken power-law synchrotron spectrum, it is possible that spatial variations in the wavelength break of the spectrum and/or a secondary synchrotron component would be able to account for the millimetre excess emission. Spatial variations in the break wavelength are expected to result in a synchrotron spectrum with multiple breaks on nebular scales. And, that is also what can be expected based on physical arguments, as the break in the synchrotron spectrum corresponds to the transition from a regime affected by synchrotron losses (shortwards of the break) to a regime without such losses. The separation between those two regimes is known to vary spatially, affecting the position of the break (see top left-hand panel of Fig. 6 in this paper, and Bandiera et al. 2002). These spatial variations of the position of the break could, however, also further smear out any bump (or excess) in the spectrum. A bump in the synchrotron spectrum depends mostly on the particle population (with a minor dependence on the source geometry and shock dynamics) and results from the pile up of energetic electrons just below the spectral break (Reynolds 2009). In our case, this would suggest a spectral break shortwards of 2 mm in the central regions of the Crab (where the excess is observed, see Section 7.1). A spectral break at mm wavelengths would imply a magnetic field several times stronger than estimated for the Crab, and demonstrates the dependence of our break wavelength on the simple broken power-law spectrum assumed to model the synchrotron emission. Attempts to model the Crab's synchrotron radiation with an evolutionary break did not improve the overall fits (see Appendix E). Due to the complexity of spatial and temporal variations in the Crab's synchrotron spectrum, we defer any further investigation of the optimal synchrotron parameters to future work.

More likely than an evolution in the energy distribution of synchrotron-emitting particles, the synchrotron radiation might originate from two different synchrotron components (Atoyan & Aharonian 1996; Bandiera et al. 2002; Meyer et al. 2010; Schweizer et al. 2013; Porth et al. 2014a; Lyutikov et al. 2018), which are thought to spatially correlate with the different particles emitting at radio and optical wavelengths. The transition between those two particle distributions is likely to occur between infrared and radio wavelengths, which might coincide with the excess emission observed in the Crab. It is however not clear whether two synchrotron components can account for the bump in the spectrum observed at mm wavelengths. Future work with increased photometric coverage in the mm, cm, and radio wavelength ranges will be required to verify whether two distinct synchrotron components could be responsible for the mm excess emission. We emphasize that the origin of the mm excess emission will not affect the dust mass inferred for the Crab Nebula in this paper. The supernova dust emission is restricted to wavebands shortwards of the SPIRE 500 μm band, while the mm excess emission hardly contributes at sub-mm wavelengths (see Table 3).

8 CONCLUSIONS

We have modelled the total integrated and resolved near-infrared to radio wavelength spectrum of the Crab Nebula with a Bayesian SED model to simultaneously account for the synchrotron radiation, IS and supernova dust emission and millimetre excess emission as observed from this PWN by *Spitzer*, *WISE*, *Herschel*, and several mm and radio ground based facilities. Here, we summarize our new results from this analysis.

(i) The contribution from IS dust emission along the line of sight to the Crab Nebula was estimated based on modelling of the ISM dust emission for regions in the vicinity of the Crab. A maximum contribution of 22 per cent was found for the SPIRE 250 μm waveband, with lower percentage contaminations in the other *Herschel* bands. The average ISM dust column corresponds to a *V*-band extinction of $A_{\rm V} = 1.08 \pm 0.38$ mag along the line of sight (see Appendix C), in agreement with the reddening inferred based on Pan-STARRS1 and 2MASS photometry (Green et al. 2015).

(ii) The resolved supernova dust mass of 0.032–0.049 $M_\odot$ (for amorphous carbon 'a-C' grains) implies that less dust has formed in the Crab Nebula than previously derived (0.11–0.24 $M_\odot$, Gomez et al. 2012). Our dust mass estimates are consistent within the uncertainties with the carbon dust masses (0.016–0.061 $M_\odot$) from Temim & Dwek (2013), and the dust mass ($0.056 \pm 0.037\,M_\odot$) reported by Nehmé et al. (2019). Unlike Temim & Dwek (2013), who ascribed their lower values to a difference in assumed dust properties, we attribute our lower dust mass estimates (compared to Gomez et al. 2012) to the corrections applied to account for IS dust emission and a reduced SPIRE 500 μm flux, which together have resulted in lower SN dust contributions at SPIRE 350 and 500 μm and consequently an average dust temperature ($T_{\rm dust} \sim 41^{+3}_{-2}$ K) for the Crab higher than was previously inferred ($T_{\rm dust} \sim$ 28–34 K, Gomez et al. 2012).

(iii) The *V*-band extinction ($A_{\rm V} = 0.20$–0.39 mag, see Fig. 7) inferred from the supernova dust mass maps is consistent with the optical extinction measurements ($A_{\rm V} = 0.20$–0.34 mag) from

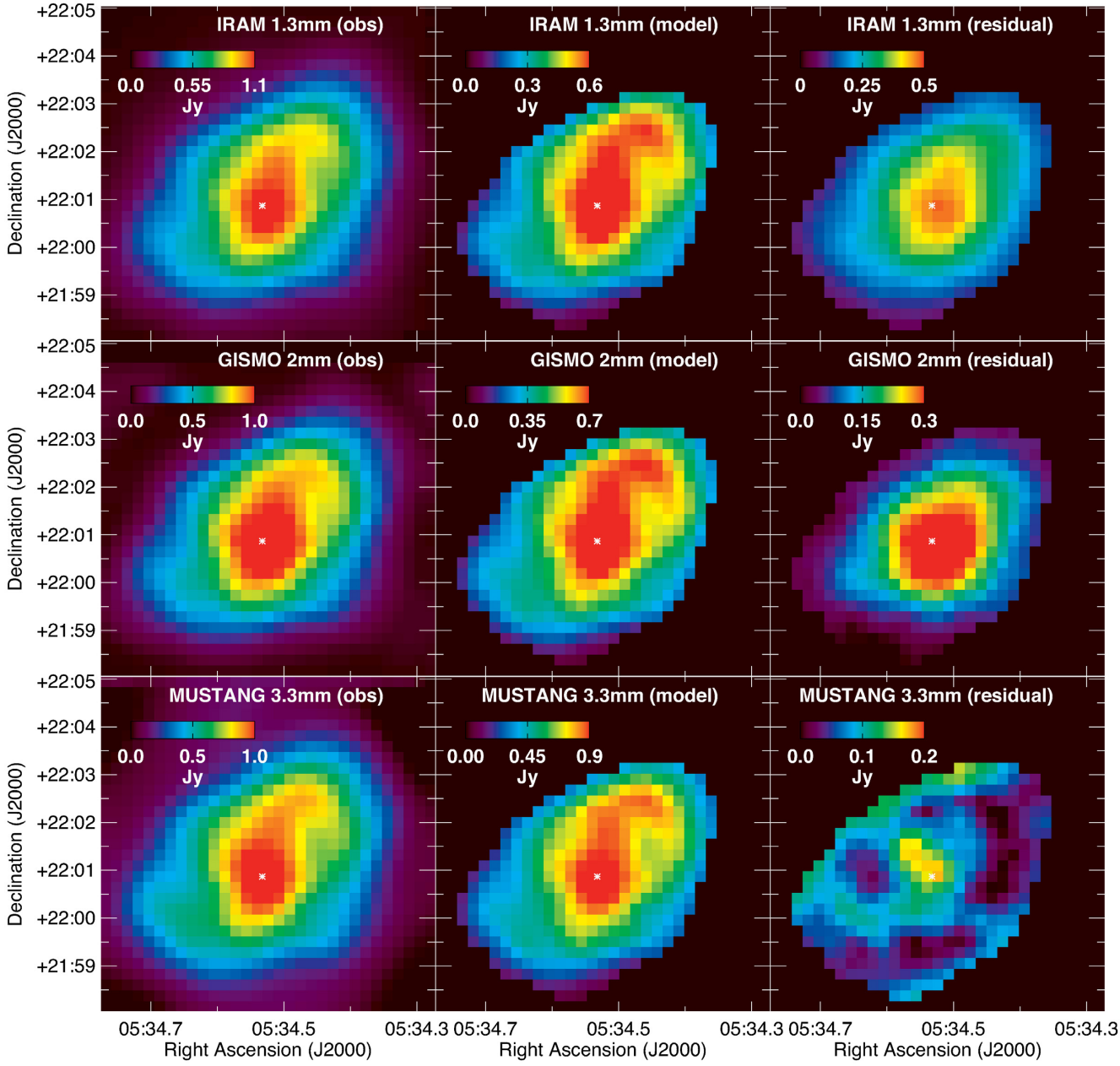

Figure 8. Resolved maps of the observed (left column), modelled (middle column), and residual (i.e. observations-model, right column) emission in three mm wavebands: MAMBO 1.3 mm (top row), GISMO 2 mm (middle row), and MUSTANG 3.3 mm (bottom row). The model emission in those mm wavebands was inferred from a Bayesian SED model on resolved scales of 14 × 14 arcsec^2 (or 0.136^2 pc^2, for a distance of 2 kpc).

Grenman et al. (2017) for seven dark globules. The dust in the Crab is predominantly found in dense filaments south of the pulsar.

(iv) If we account for the total amount of condensable material predicted to be produced by a 11 $M_\odot$ progenitor star (Woosley & Weaver 1995), we infer a dust condensation efficiency of 8–12 per cent, in line with dust condensation models for CCSNe (Nozawa et al. 2010) and consistent with dust condensation efficiencies inferred from IR/submm observations for Cas A (Priestley et al. 2019). A recently proposed revision of the Crab's distance to 3.37 kpc (Fraser & Boubert 2019) would increase our total dust mass estimate to 0.091–0.138 $M_\odot$, and imply dust condensation efficiencies of 22–33 per cent.

(v) The modelled synchrotron power-law spectrum is consistent with an average spectral index $\alpha_{\rm radio} = 0.297$ in the radio domain, a spectral break $\lambda_{\rm break}$ in the mm–cm wavelength range, and an infrared spectral index $\alpha_{\rm IR} = 0.429$.

(vi) We are unable to fit the Crab's total integrated spectrum without accounting for the observed millimetre excess emission. We investigate whether the emission is produced by electric or magnetic dipole emission originating from small spinning or magnetized grains. The spatial correlation of the excess emission with the Crab's synchrotron radiation, whereas the dust is mostly distributed along the dense filaments, does not support scenarios of spinning or magnetized grains. At the Crab's dust temperature, we would furthermore expect to observe electric and/or magnetic dipole

emission from spinning grains predominantly at FIR wavelengths. Although we cannot rule out that spinning and/or magnetized grains are responsible for the excess emission, we deem it unlikely.

(vii) Instead, we argue that the mm-wave excess emission could be affected by spatial and secular variations in the Crab's synchrotron spectrum and, more specifically, the energy distributions of relativistic particles producing the synchrotron emission. Although it is unclear how these spatial and secular variations could give rise to a bump in the spectrum. It is more plausible that the excess emission results from two distinct populations of synchrotron emitting particles driven by two different acceleration mechanisms. Future modelling efforts, with an increased number of resolved mm, cm, and longer wavelength radio observations, may be able to shed light on the origin of this excess emission.

In line with recent studies of other SNRs, we conclude that the Crab's efficient dust condensation (8–12 per cent) provides further evidence for a scenario whereby supernovae could provide considerable contributions to the IS dust budgets in galaxies. In the future, with upcoming facilities such as the James Webb Space Telescope (JWST; Gardner et al. 2006), SPICA (Roelfsema et al. 2018), and the Origins Space Telescope, we will be able to expand on the current sample of PWNe with dust mass detections and, at the same time, look for dust features characteristic of the type of grain species formed in PWNe, which will help to further bring down uncertainties on current supernova dust masses and to provide observational input to test the nucleation of various grain species during the first couple of hundred days post-explosion in the current generation of core-collapse supernova dust models (see Sarangi, Matsuura & Micelotta 2018 for a recent review).

ACKNOWLEDGEMENTS

The authors would like to thank the anonymous referee for her/his useful suggestions that have significantly improved the discussion and the presentation of our results. The authors would like to thank Rick Arendt for kindly sharing his mm data (GISMO 2 mm and MUSTANG 3.3 mm) of the Crab Nebula; and Isabella Lamperti, Anthony Jones, Bruce Draine and Boris Leistedt for fruitful discussions. IDL gratefully acknowledges the support of the Research Foundation Flanders (FWO). MJB, AB, and RW acknowledge support from European Research Council (ERC) Advanced Grant SNDUST 694520. MM acknowledges support from STFC Ernest Rutherford fellowship (ST/L003597/1). HLG and HC acknowledges support from the European Research Council (ERC) in the form of Consolidator Grant CosmicDust. FP acknowledges support from the UK Science and Technology Funding Council (STFC).

PACS was developed by a consortium of institutes led by MPE (Germany) and including UVIE (Austria); KU Leuven, CSL, IMEC (Belgium); CEA, LAM (France); MPIA (Germany); INAFIFSI/ OAA/OAP/OAT, LENS, SISSA (Italy); IAC (Spain). This development has been sup- ported by the funding agencies BMVIT (Austria), ESA- PRODEX (Belgium), CEA/CNES (France), DLR (Ger- many), ASI/INAF (Italy), and CICYT/ MCYT (Spain). SPIRE was developed by a consortium of institutes led by Cardiff University (UK) and including Univ. Lethbridge (Canada); NAOC (China); CEA, LAM (France); IFSI, Univ. Padua (Italy); IAC (Spain); Stockholm Observatory (Sweden); Imperial College London, RAL, UCL-MSSL, UKATC, Univ. Sussex (UK); and Caltech, JPL, NHSC, Univ. Colorado (USA). This development has been supported by national funding agencies: CSA (Canada); NAOC (China); CEA, CNES, CNRS (France); ASI (Italy); MCINN (Spain); SNSB (Sweden); STFC and UKSA (UK); and NASA (USA).

REFERENCES

Aller H. D., Reynolds S. P., 1985, ApJ, 293, L73
Aniano G., Draine B. T., Gordon K. D., Sandstrom K., 2011, PASP, 123, 1218
Arendt R. G. et al., 2011, ApJ, 734, 54
Arendt R. G., Dwek E., Kober G., Rho J., Hwang U., 2014, ApJ, 786, 55
Atoyan A. M., Aharonian F. A., 1996, MNRAS, 278, 525
Baars J. W. M., Genzel R., Pauliny-Toth I. I. K., Witzel A., 1977, A&A, 61, 99
Balog Z. et al., 2014, Exp. Astron., 37, 129
Bandiera R., Neri R., Cesaroni R., 2002, A&A, 386, 1044
Barlow M. J. et al., 2010, A&A, 518, L138
Bendo G. J. et al., 2013, MNRAS, 433, 3062
Bevan A. et al., 2019, MNRAS, 485, 5192
Bevan A., Barlow M. J., 2016, MNRAS, 456, 1269
Bevan A., Barlow M. J., Milisavljevic D., 2017, MNRAS, 465, 4044
Bietenholz M. F., Kronberg P. P., 1990, ApJ, 357, L13
Bietenholz M. F., Kronberg P. P., 1991, ApJ, 368, 231
Bietenholz M. F., Kassim N., Frail D. A., Perley R. A., Erickson W. C., Hajian A. R., 1997, ApJ, 490, 291
Bietenholz M. F., Yuan Y., Buehler R., Lobanov A. P., Blandford R., 2015, MNRAS, 446, 205
Blair W. P., Long K. S., Vancura O., Bowers C. W., Conger S., Davidsen A. F., Kriss G. A., Henry R. B. C., 1992, ApJ, 399, 611
Bucciantini N., Arons J., Amato E., 2011, MNRAS, 410, 381
Chawner H. et al., 2019, MNRAS, 483, 70
Chevalier R. A., 1977, in Schramm D. N., ed., Astrophysics and Space Science Library, Vol. 66, Supernovae. Springer-Verlag, Berlin, p. 53
Davidson K., 1979, ApJ, 228, 179
De Looze I., Barlow M. J., Swinyard B. M., Rho J., Gomez H. L., Matsuura M., Wesson R., 2017, MNRAS, 465, 3309
Dicker S. R. et al., 2008, in Duncan W. D., Holland W. S., Withington S., Zmuidzinas J., eds, Proc. SPIE Conf. Ser. Vol. 7020, Millimeter and Submillimeter Detectors and Instrumentation for Astronomy IV. SPIE, Bellingham, p. 702005
Dorschner J., Begemann B., Henning T., Jaeger C., Mutschke H., 1995, A&A, 300, 503
Dubner G., Castelletti G., Kargaltsev O., Pavlov G. G., Bietenholz M., Talavera A., 2017, ApJ, 840, 82
Dwek E., Galliano F., Jones A. P., 2007, ApJ, 662, 927
Engelbracht C. W. et al., 2007, PASP, 119, 994
Fazio G. G. et al., 2004, ApJS, 154, 10
Fitzpatrick E. L., 1999, PASP, 111, 63
Fraser M., Boubert D., 2019, ApJ, 871, 92
Gall C. et al., 2014, Nature, 511, 326
Gardner J. P. et al., 2006, Space Sci. Rev., 123, 485
Gomez H. L. et al., 2012, ApJ, 760, 96
Gordon K. D. et al., 2007, PASP, 119, 1019
Graham J. R., Wright G. S., Longmore A. J., 1990, ApJ, 352, 172
Green D. A., Tuffs R. J., Popescu C. C., 2004, MNRAS, 355, 1315
Green G. M. et al., 2015, ApJ, 810, 25
Grenman T., Gahm G. F., Elfgren E., 2017, A&A, 599, A110
Groenewegen M. A. T. et al., 2011, A&A, 526, A162
Hashimoto T. et al., 2018, Nature, 557, 392
Hester J. J., 2008, ARA&A, 46, 127
Houck J. R. et al., 2004, in Mather J. C., ed., Proc. SPIE Conf. Ser. Vol. 5487, Optical, Infrared, and Millimeter Space Telescopes. SPIE, Bellingham, p. 62
Indebetouw R. et al., 2014, ApJ, 782, L2
Jäger C., Dorschner J., Mutschke H., Posch T., Henning T., 2003, A&A, 408, 193
Jarrett T. H. et al., 2013, AJ, 145, 6

Jones A. P., 2012a, A&A, 540, A1
Jones A. P., 2012b, A&A, 540, A2
Jones A. P., 2012c, A&A, 542, A98
Jones A. P., Fanciullo L., Köhler M., Verstraete L., Guillet V., Bocchio M., Ysard N., 2013, A&A, 558, A62
Jun B.-I., 1998, ApJ, 499, 282
Kennel C. F., Coroniti F. V., 1984, ApJ, 283, 710
Laporte N. et al., 2017, ApJ, 837, L21
Lawrence S. S., MacAlpine G. M., Uomoto A., Woodgate B. E., Brown L. W., Oliversen R. J., Lowenthal J. D., Liu C., 1995, AJ, 109, 2635
Lebouteiller V., Barry D. J., Spoon H. W. W., Bernard-Salas J., Sloan G. C., Houck J. R., Weedman D. W., 2011, ApJS, 196, 8
Loh E. D., Baldwin J. A., Ferland G. J., 2010, ApJ, 716, L9
Loh E. D., Baldwin J. A., Curtis Z. K., Ferland G. J., O'Dell C. R., Fabian A. C., Salomé P., 2011, ApJS, 194, 30
Loh E. D., Baldwin J. A., Ferland G. J., Curtis Z. K., Richardson C. T., Fabian A. C., Salomé P., 2012, MNRAS, 421, 789
Lyutikov M., Temim T., Komissarov S., Slane P., Sironi L., Comisso L., 2018, preprint (arXiv:1811.01767)
MacAlpine G. M., Satterfield T. J., 2008, AJ, 136, 2152
MacAlpine G. M., Ecklund T. C., Lester W. R., Vanderveer S. J., Strolger L.-G., 2007, AJ, 133, 81
Macías-Pérez J. F., Mayet F., Aumont J., Désert F.-X., 2010, ApJ, 711, 417
Madsen K. K. et al., 2015, ApJ, 801, 66
Marassi S., Schneider R., Limongi M., Chieffi A., Graziani L., Bianchi S., 2019, MNRAS, 484, 2587
Marsden P. L., Gillett F. C., Jennings R. E., Emerson J. P., de Jong T., Olnon F. M., 1984, ApJ, 278, L29
Matsuura M. et al., 2011, Science, 333, 1258
Matsuura M. et al., 2015, ApJ, 800, 50
Meyer M., Horns D., Zechlin H.-S., 2010, A&A, 523, A2
Miller J. S., 1973, ApJ, 180, L83
Miller J. S., 1978, ApJ, 220, 490
Morgan H. L., Edmunds M. G., 2003, MNRAS, 343, 427
Nehmé C., Kassounian S., Sauvage M., 2019, preprint (arXiv:e-print)
Nozawa T., Kozasa T., Habe A., 2006, ApJ, 648, 435
Nozawa T., Kozasa T., Tominaga N., Maeda K., Umeda H., Nomoto K., Krause O., 2010, ApJ, 713, 356
Omand C. M. B., Kashiyama K., Murase K., 2019, MNRAS, 484, 5468
Ott S., 2010, in Mizumoto Y., Morita K.-I., Ohishi M., eds, ASP Conf. Ser., Vol. 434, Astronomical Data Analysis Software and Systems XIX. Astron. Soc. Pac., San Francisco, p. 139
Owen P. J., Barlow M. J., 2015, ApJ, 801, 141
Pilbratt G. L. et al., 2010, A&A, 518, L1
Planck Collaboration XXXI, 2016a, A&A, 586, A134
Planck Collaboration XXVI, 2016b, A&A, 594, A26
Porth O., Komissarov S. S., Keppens R., 2014a, MNRAS, 438, 278
Porth O., Komissarov S. S., Keppens R., 2014b, MNRAS, 443, 547
Priestley F. D., Barlow M. J., De Looze I., 2019, MNRAS, 485, 440
Raymond J. C., Koo B.-C., Lee Y.-H., Milisavljevic D., Fesen R. A., Chilingarian I., 2018, ApJ, 866, 128
Reynolds S. P., 2009, ApJ, 703, 662
Rho J. et al., 2008, ApJ, 673, 271
Rho J. et al., 2018, MNRAS, 479, 5101
Rieke G. H. et al., 2004, ApJS, 154, 25
Roelfsema P. R. et al., 2018, Publ. Astron. Soc. Aust., 35, e030
Rouleau F., Martin P. G., 1991, ApJ, 377, 526
Roussel H., 2013, PASP, 125, 1126
Sankrit R. et al., 1998, ApJ, 504, 344
Sankrit R., Hester J. J., 1997, ApJ, 491, 796
Sarangi A., Cherchneff I., 2015, A&A, 575, A95
Sarangi A., Matsuura M., Micelotta E. R., 2018, Space Sci. Rev., 214, 63
Satterfield T. J., Katz A. M., Sibley A. R., MacAlpine G. M., Uomoto A., 2012, AJ, 144, 27
Schweizer T., Bucciantini N., Idec W., Nilsson K., Tennant A., Weisskopf M. C., Zanin R., 2013, MNRAS, 433, 3325
Seward F. D., Tucker W. H., Fesen R. A., 2006, ApJ, 652, 1277
Sluder A., Milosavljević M., Montgomery M. H., 2018, MNRAS, 480, 5580
Smith N., 2003, MNRAS, 346, 885
Smith N., 2013, MNRAS, 434, 102
Staguhn J. G. et al., 2006, in Zmuidzinas J., Holland W. S., Withington S., Duncan W. D., eds, Proc. SPIE Conf. Ser. Vol. 6275, Millimeter and Submillimeter Detectors and Instrumentation for Astronomy III. SPIE, Bellingham. p. 62751D
Temim T. et al., 2006, AJ, 132, 1610
Temim T., Dwek E., 2013, ApJ, 774, 8
Temim T., Sonneborn G., Dwek E., Arendt R. G., Gehrz R. D., Slane P., Roellig T. L., 2012, ApJ, 753, 72
Temim T., Dwek E., Arendt R. G., Borkowski K. J., Reynolds S. P., Slane P., Gelfand J. D., Raymond J. C., 2017, ApJ, 836, 129
Todini P., Ferrara A., 2001, MNRAS, 325, 726
Trimble V., 1968, AJ, 73, 535
Velusamy T., Roshi D., Venugopal V. R., 1992, MNRAS, 255, 210
Veron-Cetty M. P., Woltjer L., 1993, A&A, 270, 370
Vinyaikin E. N., 2007, Astron. Rep., 51, 570
Watson D., Christensen L., Knudsen K. K., Richard J., Gallazzi A., Michałowski M. J., 2015, Nature, 519, 327
Weiland J. L. et al., 2011, ApJS, 192, 19
Werner M. W. et al., 2004, ApJS, 154, 1
Wesson R., Barlow M. J., Matsuura M., Ercolano B., 2015, MNRAS, 446, 2089
Willingale R., Aschenbach B., Griffiths R. G., Sembay S., Warwick R. S., Becker W., Abbey A. F., Bonnet-Bidaud J.-M., 2001, A&A, 365, L212
Woltjer L., 1987, in Pacini F., ed., NATO Advanced Science Institutes (ASI) Series C, Vol. 195. D. Reidel Publishing Co., Dordrecht, p. 209
Woosley S. E., Weaver T. A., 1995, ApJS, 101, 181
Wright E. L. et al., 2010, AJ, 140, 1868
Zubko V. G., Mennella V., Colangeli L., Bussoletti E., 1996, MNRAS, 282, 1321

SUPPORTING INFORMATION

Supplementary data are available at *MNRAS* online.

Appendix A: BAYESIAN SED MODELLING APPROACH
Appendix B: RESOLVED BAYESIAN MODEL RESIDUALS
Appendix C: GALACTIC DUST EMISSION
Appendix D: ALTERNATIVE EXPLANATIONS FOR THE MM EXCESS EMISSION IN THE CRAB
Appendix E: EVOLUTIONARY SYNCHROTRON SPECTRUM

Please note: Oxford University Press is not responsible for the content or functionality of any supporting materials supplied by the authors. Any queries (other than missing material) should be directed to the corresponding author for the article.

This paper has been typeset from a TEX/LATEX file prepared by the author.